

# SEPARABLE SOLUTIONS OF FORCE-FREE SPHERES AND APPLICATIONS TO SOLAR ACTIVE REGIONS

A. Prasad, A. Mangalam and B. Ravindra

*Indian Institute of Astrophysics,  
Sarjapur Road, Koramangala 2nd Block, Bangalore 560034, India*

avijeet@iiap.res.in, mangalam@iiap.res.in, ravindra@iiap.res.in

## ABSTRACT

In this paper, we present a systematic study of the force-free field equation for simple axisymmetric configurations in spherical geometry and apply it to the solar active regions. The condition of separability of solutions in the radial and angular variables leads to two classes of solutions: linear and nonlinear force-free fields. We have studied these linear solutions and extended the nonlinear solutions for the radial power law index to the irreducible rational form  $n = p/q$ , which is allowed for all cases of odd  $p$  and cases of  $q > p$  for even  $p$ , where the poloidal flux  $\psi \propto 1/r^n$  and field  $\mathbf{B} \propto 1/r^{n+2}$ . We apply these solutions to simulate photospheric vector magnetograms obtained using the spectropolarimeter on board *Hinode*. The effectiveness of our search strategy is first demonstrated on test inputs of dipolar, axisymmetric, and non axisymmetric linear force-free fields. Using the best-fit to these magnetograms, we build three-dimensional axisymmetric field configurations and calculate the energy and relative helicity with two independent methods, which are in agreement. We have analyzed five magnetograms for AR 10930 spanning a period of three days during which two X-class flares occurred which allowed us to find the free energy and relative helicity of the active region before and after the flare; our analysis indicates a peak in these quantities before the flare events which is consistent with the results mentioned in literature. We also analyzed single-polarity regions AR 10923 and 10933, which showed very good fits with potential fields. This method can provide useful reconstruction of the nonlinear force-free (NLFF) fields as well as reasonably good input fields for other numerical techniques.

*Subject headings:* magnetohydrodynamics (MHD)-Sun: activity-Sun: corona-Sun: flares -Sun: magnetic fields sunspots

## 1. INTRODUCTION

The active regions in the solar photosphere are locations of high magnetic field where magnetic pressure starts to dominate over gas pressure. In such conditions the plasma is likely to follow

a force-free equation of state, where the Lorentz force vanishes at all points. It was shown by Taylor (1974) that in systems where magnetic forces are dominant in the presence of kinematic viscosity, linear force-free fields are natural end configurations. A more general class of force-free fields is obtained when the energy of the system is minimized with constraints of total mass, angular momentum, cross helicity and relative helicity (e.g., Finn & Antonsen (1983); Mangalam & Krishan (2000)). Within the context of force-free configurations, there are numerous possibilities that can be obtained due to underlying geometry and symmetry of the problem in addition to the invariants involved. There have been several attempts to construct such full three-dimensional (3D) models from two-dimensional (2D) data obtained at one level vector magnetograms. A summary of the various numerical techniques are discussed in Schrijver et al. (2006) and Metcalf et al. (2008). They compare six algorithms for the computation of nonlinear force-free (NLFF) magnetic fields, which include optimization (Wheatland et al. 2000; Wiegelmann 2004; Wiegelmann et al. 2006), magnetofrictional (Yang et al. 1986; McClymont & Mikic 1994; Roumeliotis 1996; McClymont et al. 1997), GradRubin based (Grad & Rubin 1958; Amari et al. 1997, 2006; Wheatland 2007; Wheatland & Régnier 2009; Wheatland & Leka 2010), and Greens function-based methods (Yan & Sakurai 1997, 2000; Yan 2005; Yan & Li 2006) by evaluating their performance in tests on analytical force-free field models for which boundary conditions are specified either for the entire surface area of a cubic volume or for an extended lower boundary. Figures of merit were used to compare the input vector field to the resulting model fields. Based on these, they argue that all algorithms yield NLFF fields that agree best with the input field in the lower central region of the volume, where the field and electrical currents are strongest and the effects of boundary conditions the weakest. The NLFF codes when applied to solar data, do not necessarily converge to a single solution. To address this Wheatland & Leka (2011) include uncertainties on the electric current densities at the boundaries iteratively until the two nonlinear solutions agree, leading to a more reliable construction.

Because the NLFF techniques require good input fields for fast convergence and are subject to uncertainties at the boundary conditions that propagate during extrapolation, we are exploring fits of the data directly to analytic solutions. The best-fit to a well-known (non)linear (semi)analytic solution would give us more insight into the kind of structure that could be present in the volume given an optimal correlation with the fields observed on the magnetogram. The solution thus found can then be exploited to yield quantities of interest such as relative helicity and free energy that can be computed for the 3D configuration. Further, one can explore the stability and dynamics of these structures at a later stage.

Whereas there are several possible topologies for various geometries and boundary conditions, e.g., Marsh (1996), it is our goal here to take the simplest geometric approach of a sphere. We show that separability condition leads to two classes of solutions: linear and nonlinear force-free fields. We call these linear fields as Chandrasekhar solution (Chandrasekhar 1956), hereafter referred to as C modes and the nonlinear fields as Low-Lou solutions (Low & Lou 1990), hereafter referred to as LL modes. These computationally cheap 3D analytic models are comparable with other numerics

or with observations and this allows us to make more precise predictions of the physically relevant configurations. Because the validity of physical assumptions can vary from active region to active region, we restrict ourselves to exploring the most simplest of solutions involving the least number of parameters, namely the choice of the modes and the two of the three Euler angles that will represent any arbitrary rotation of the configuration space into the coordinates of the observed magnetogram. An outline of this approach was previously presented in Prasad & Mangalam (2013).

The paper is presented as follows: In Section 2 we describe the formulation of the free energy and relative helicity in a shell geometry. In Section 3, we show that the force-free field equation under assumption of axisymmetry leads to linear (C modes) and nonlinear (LL modes) force-free fields which are discussed in Section 4 and Section 5, respectively. In Section 6, we present the construction of magnetogram templates and the search strategy for obtaining the best-fit using suitable fitting parameters. In Section 7 and Section 8 we present the data used for this study and compare them with the simulated models. The summary and conclusions are presented in Section 9. Details of mathematical derivations for some of the relations are in the Appendices A-H. Table 6 provides a formulary for the C and LL modes.

## 2. FORMULATION OF THE FREE ENERGY AND RELATIVE HELICITY IN SHELL GEOMETRY

In this paper, we study the solutions of axisymmetric linear and NLFFs in a spherical shell geometry and calculate the relevant quantities like free energy and relative helicity for these configurations. The free energy of the system is the difference between the energies of a force-free field and a potential field in the entire volume. The expression for free energy  $E_{\text{free}}$  is given by

$$E_{\text{free}} = E_{\text{ff}} - E_P, \quad (1)$$

where  $E_{\text{ff}}$  and  $E_P$  are the energies of the force-free field and the potential field, respectively. Because the potential field is the minimum energy configuration for a given boundary condition,  $E_{\text{free}}$  is always positive. Relative helicity is a gauge-invariant measure of linkages between the field lines with respect to a potential field matching to the perpendicular field at the surface (Berger & Field 1984). Relative helicity can be computed using the Finn–Antonsen formula (Finn & Antonsen 1985)

$$H_{\text{rel}} = \int_V (\mathbf{A} + \mathbf{A}_P) \cdot (\mathbf{B} - \mathbf{B}_P) dV, \quad (2)$$

where  $\mathbf{A}_P$  and  $\mathbf{B}_P$  are the vector potential and magnetic field for the potential field with the constraint that  $(\mathbf{B}_P)_r = \mathbf{B}_r$ , where  $r$  represents the radius at the boundary. Another expression that can be used for calculating relative helicity in spherical geometry that is independent of the potential field follows the treatment given in Berger (1985), where

$$H_{\text{rel}} = 2 \int_V \mathbf{L}P \cdot \mathbf{L}T dV, \quad (3)$$

$\mathbf{L} = -\mathbf{r} \times \nabla$  is the angular momentum operator, and  $P$  and  $T$  are the poloidal and toroidal components of the magnetic field respectively. The expression in Equation (3) can be further simplified for axisymmetric magnetic fields in spherical geometry. The toroidal component  $\mathbf{L}T = B_\phi \hat{\phi}$ , whereas  $\mathbf{L}P = A_\phi \hat{\phi} + \nabla\psi$ , which includes the gauge term  $\nabla\psi$ ;  $A_\phi$  and  $B_\phi$  are the  $\phi$  components of the vector potential and the magnetic field. We now use the gauge invariance of Equation (3) to get the final expression for relative helicity to be

$$\int_V \mathbf{L}P \cdot \mathbf{L}T dV = \int_V A_\phi B_\phi dV + \int_V \nabla\psi \cdot (B_\phi \hat{\phi}) dV. \quad (4)$$

The last term in the right-hand side of Equation (4) vanishes as

$$\int_V \nabla\psi \cdot (B_\phi \hat{\phi}) dV = \int_V \nabla \cdot (\psi B_\phi \hat{\phi}) dV = \int_S (\psi B_\phi) \hat{\phi} \cdot \hat{r} dS = 0. \quad (5)$$

Thus Equation (4) simplifies to

$$H_{\text{rel}} = 2 \int_V A_\phi B_\phi dV. \quad (6)$$

In the above derivation, it is seen that  $\mathbf{L}P$  and  $\mathbf{L}T$  are parallel to each other and perpendicular to the surface normal, which leads to  $H_{\text{rel}}$  being independent of the choice of  $\psi$ . This is peculiar only to certain geometries like spherical and planar. Also see Low (2006), where an absolute helicity is derived independent of the potential field in the special geometries that employ Euler potentials. In the case of the linear models used here (C modes; Section 4) the energy and helicity are finite and in the case of the nonlinear model used here (LL modes; Section 5),  $\mathbf{B} \propto r^{-n-2}$  ( $n > 1$ ) and energy and helicity show singular behavior at the origin.

### 3. AXISYMMETRIC SEPARABLE LINEAR AND NONLINEAR FORCE-FREE FIELDS

The force-free magnetic field  $\mathbf{B}$  is described by the equation

$$\nabla \times \mathbf{B} = \alpha \mathbf{B} \quad (7)$$

from which it follows that  $\mathbf{B} \cdot \nabla \alpha = 0$ . This requires  $\alpha$  to be a constant along the magnetic field lines. Following the treatment in Low & Lou (1990), we assume an axisymmetric magnetic field configuration and express it in terms of two scalar functions  $\psi$  and  $Q(\psi)$  in spherical polar coordinates:

$$\mathbf{B} = \frac{1}{r \sin \theta} \left( \frac{1}{r} \frac{\partial \psi}{\partial \theta} \hat{\mathbf{r}} - \frac{\partial \psi}{\partial r} \hat{\boldsymbol{\theta}} + Q \hat{\boldsymbol{\phi}} \right), \quad (8)$$

which is divergence-free by construction. For an orthonormal coordinate system with a metric defined as  $ds^2 = g_{ii} dx^i dx^i$ , the line element along the magnetic field line  $dl$  is given by  $\hat{\mathbf{l}} = \sqrt{g_{ii}} \frac{dx^i}{ds} \hat{\mathbf{i}} = \frac{B_i}{|\mathbf{B}|} \hat{\mathbf{i}}$ ; hence  $\frac{\sqrt{g_{ii}} dx^i}{B_i}$  represents the equation for lines of force, and applying this



in axisymmetry gives  $\psi = \text{const.}$ , whose contours represent the poloidal field lines. Combining the Equations 7 and 8, we obtain

$$\alpha = \frac{dQ}{d\psi} \quad (9)$$

and

$$\frac{\partial^2 \psi}{\partial r^2} + \frac{(1 - \mu^2)}{r^2} \frac{\partial^2 \psi}{\partial \mu^2} + Q \frac{dQ}{d\psi} = 0, \quad (10)$$

where  $\mu = \cos \theta$ . To solve the above equation we choose a separable form of the type

$$\psi = f(r)P(\mu), \quad Q = a\psi^\beta, \quad (11)$$

where  $f$  and  $P$  are scalar functions of  $r$  and  $\mu$ , respectively;  $a$  and  $\beta$  are constants. Combining Equations (10) and (11), it follows that

$$r^2 \frac{f''}{f} + (1 - \mu^2) \frac{P''}{P} + a^2 \beta r^2 f^{2\beta-2} P^{2\beta-2} = 0. \quad (12)$$

The first term in the left-hand side of the above equation is a function of  $r$  alone and the second term is that of  $\mu$  alone. The resulting two possibilities for obtaining separable solutions are that the third term be a function of either

- (a)  $r$  alone, which is satisfied if  $\beta = 1$ ; these solutions were presented in Chandrasekhar (1956), and we refer to them as C modes, or
- (b)  $\mu$  alone, which is satisfied if  $r^2 f^{2\beta-2} = 1$ ; these solutions were partially explored by Low & Lou (1990) and are termed here as LL modes.

#### 4. The $\beta = 1$ case: C modes

The C modes pertain to the linear force-free fields because the condition  $\beta = 1$  along with Equation (9) imply  $\alpha = a$ , and it follows from Equation (12) that

$$r^2 \frac{f''}{f} + a^2 r^2 + (1 - \mu^2) \frac{P''}{P} = 0. \quad (13)$$

The radial part of the above equation is given by

$$r^2 \frac{f''}{f} + a^2 r^2 = n'(n' + 1) \quad (14)$$

where  $n'$  is a constant whose solutions are

$$f_{n'}(r) = c_1 \sqrt{r} J_{(1+2n')/2}(ar) + c_2 \sqrt{r} Y_{(1+2n')/2}(ar) \quad (15)$$

where  $J$  and  $Y$  are cylindrical Bessel functions;  $c_1$  and  $c_2$  are constants to be determined from the boundary conditions. The angular part of Equation (13) is given by

$$(1 - \mu^2) \frac{P''}{P} = -n'(n' + 1), \quad (16)$$

whose solution is given by

$$P(\mu) = (1 - \mu^2)^{1/2} P_{n'}^1(\mu), \quad (17)$$

where  $P_{n'}^1$  is the associated Legendre function of the first kind for integer  $n'$ . This solution is equivalent to that obtained in Chandrasekhar (1956), and the following equations give the correspondence between the solutions

$$\begin{aligned} a &\leftrightarrow \alpha \\ f_{n'}(r) &\leftrightarrow \sqrt{r} g_{m+3/2}(\alpha r) \\ P_{n'}^1(\mu) &\leftrightarrow -(1 - \mu^2)^{1/2} C_m^{3/2}(\mu) \\ n' &\leftrightarrow m + 1 \end{aligned} \quad (18)$$

where  $C_m^{3/2}(\mu)$  denotes the Gegenbauer polynomial and  $g_{m+3/2}(\alpha r)$  represents any arbitrary linear combination of the cylindrical Bessel functions  $J_{m+3/2}(\alpha r)$  and  $Y_{m+3/2}(\alpha r)$ . Henceforth for the calculations of C modes we will be using the expressions from Chandrasekhar (1956). Now  $\psi$  can be rewritten as

$$\psi = f(r)P(\mu) = f_{n'}(r)(1 - \mu^2)^{1/2} P_{n'}^1(\mu) = r^2 S_m(r)(1 - \mu^2), \quad (19)$$

where

$$S_m = \frac{g_{m+3/2}(\alpha r)}{r^{3/2}} C_m^{3/2}(\mu). \quad (20)$$

The application of these solutions to the case of finite spheres under suitable boundary conditions is discussed in Section A. The above expression can be further simplified by substituting for  $S_m$  using Equations (20) and (A3) to

$$\begin{aligned} \mathbf{B} = & \left( \frac{-J_{m+3/2}(\alpha r)}{r^{3/2}} \frac{d}{d\mu} [(1 - \mu^2) C_m^{3/2}(\mu)], \right. \\ & \left. \frac{-1}{r} \frac{d}{dr} [r^{1/2} J_{m+3/2}(\alpha r)] (1 - \mu^2)^{1/2} C_m^{3/2}(\mu), \frac{\alpha J_{m+3/2}(\alpha r)}{r^{1/2}} (1 - \mu^2)^{1/2} C_m^{3/2}(\mu) \right). \end{aligned} \quad (21)$$

The derivation for the potential field corresponding to Equation (A5) is given in Appendix C. The final expressions for the potential field is found to be

$$\mathbf{B}_P = \left( \left[ (m+1)a_{m+1}r^m - \frac{(m+2)b_{m+1}}{r^{m+3}} \right] P_{m+1}(\mu), -(1 - \mu^2)^{1/2} \left[ a_{m+1}r^m + \frac{b_{m+1}}{r^{m+3}} \right] \frac{dP_{m+1}}{d\mu}, 0 \right). \quad (22)$$

$P_{(m+1)}(\mu)$  are the Legendre polynomials, where the coefficients are calculated to be

$$\chi_l = \chi_{m+1}(r_1) = \frac{(m+1)(m+2)}{r_1^{3/2}} J(m+3/2, \alpha r_1) \quad (23)$$

$$\begin{aligned} a_l = a_{m+1} &= \frac{\chi_{m+1}(r_1)}{(m+1)} \frac{r_1^{m+3}}{r_1^{2m+3} - r_2^{2m+3}} \\ b_l = b_{m+1} &= \frac{(m+1)}{(m+2)} a_{m+1} r_2^{(2m+3)} \end{aligned} \quad (24)$$

For the general case of open field lines, where the field has a nonzero normal component at the boundaries, the energy of the force-free field is given by

$$E_{\text{ff}}(\alpha, n, m, r_1, r_2) = \frac{1}{4} \int_{r_1}^{r_2} \int_{-1}^1 (B_r^2 + B_\theta^2 + B_\phi^2) r^2 dr d\mu. \quad (25)$$

Upon evaluation, the above equation takes the following form

$$\begin{aligned} E_{\text{ff}}(\alpha, n, m, r_1, r_2) &= \frac{(m+1)(m+2)}{2(2m+3)} \left[ 2 \int_{r_1}^{r_2} \alpha^2 r J_{m+3/2}^2(\alpha r) dr \right. \\ &\quad \left. - r_1^{1/2} J_{m+3/2}(\alpha r_1) \frac{d}{dr} \{ r^{1/2} J_{m+3/2}(\alpha r) \} \Big|_{r=r_1} \right] \end{aligned} \quad (26)$$

An alternative and equivalent expression for the energy can also be obtained from Equation (B2), from which  $E_{\text{ff}} = E_v(r_2) - E_v(r_1)$ , where

$$E_v(r) = \frac{(m+1)(m+2)}{2(2m+3)} \left[ r \left[ \frac{d}{dr} \left\{ r^{1/2} J_{m+3/2}(\alpha r) \right\} \right]^2 + \{ \alpha^2 r^2 - (m+1)(m+2) \} J_{m+3/2}^2(\alpha r) \right]. \quad (27)$$

We have verified that Equations (27) and (26) are analytically equivalent through the use of Equation (14) and algebraic manipulation of Bessel identities. In order to calculate the free energy of the configuration using Equation (1), we compute the energy of the potential field constructed from this force-free field (see Appendix C.1) which is given by

$$\begin{aligned} E_{\text{pot}}(m, r_1, r_2) &= \frac{1}{2(2m+3)} \int_{r_1}^{r_2} \left[ \left( (m+1)a_{m+1}r^{m+1} - \frac{(m+2)b_{m+1}}{r^{m+2}} \right)^2 \right. \\ &\quad \left. + (m+1)(m+2) \left( a_{m+1}r^{m+1} + \frac{b_{m+1}}{r^{m+2}} \right)^2 \right] dr. \end{aligned} \quad (28)$$

We now calculate the relative helicity of the configuration using Equation (2). The relevant quantities to be calculated for this purpose are the vector potentials for the force-free field  $\mathbf{A}$  and that of the potential field  $\mathbf{A}_P$ . We use gauge freedom for the vector potential to write  $\mathbf{A} = \mathbf{B}/\alpha$ . The vector potential for the potential field is calculated in Appendix D, and is given by

$$\mathbf{A}_P = \left( 0, 0, (1 - \mu^2)^{1/2} P'_{m+1}(\mu) \left[ \frac{a_{m+1}r^{m+1}}{m+2} - \frac{b_{m+1}}{(m+1)r^{m+2}} \right] \right). \quad (29)$$

The relative helicity for region *II* can be written as

$$\begin{aligned}
H_{rel}(\alpha, n, m, r_1, r_2) &= \int \left( \frac{B^2}{\alpha} + \mathbf{A}_P \cdot \mathbf{B} - \frac{\mathbf{B}}{\alpha} \cdot \mathbf{B}_P \right) dV \\
&= \frac{8\pi E_{\text{ff}}}{\alpha} + \frac{4\pi(m+1)(m+2)}{\alpha(2m+3)} \left[ \alpha^2 \int_{r_1}^{r_2} \left( \frac{a_{m+1}r^{m+1}}{m+2} - \frac{b_{m+1}}{(m+1)r^{m+2}} \right) r^{3/2} J_{m+3/2}(\alpha r) dr \right. \\
&\quad \left. + r_1^{1/2} \left( a_{m+1}r_1^{m+1} + \frac{b_{m+1}}{r_1^{m+2}} \right) J_{m+3/2}(\alpha r_1) \right]. \tag{30}
\end{aligned}$$

An equivalent formula for the relative helicity obtained using Equation (6) works out to be

$$H_{rel}(\alpha, n, m, r_1, r_2) = \frac{2}{\alpha} \int_V B_\phi^2 dV = \frac{8\pi\alpha(m+1)(m+2)}{2m+3} \int_{r_1}^{r_2} r J_{m+3/2}^2(\alpha r) dr. \tag{31}$$

The analytical equivalence of Equations (30) and (31) is presented in Appendix F.1.

## 5. THE $r^2 f^{2\beta-2} = 1$ CASE: LL MODES

We now study the second set of solutions obtained in Section 3: the LL modes. The condition  $r^2 f^{2\beta-2} = 1$  along with Equation (12) imply

$$f^{\beta-1} = r^{-1}. \tag{32}$$

Assuming the functional form

$$f(r) = r^{-n}, \tag{33}$$

where  $n$  is a constant, gives the condition  $\beta = (n+1)/n$ , and Equation (12) then yields the following equation as obtained by Low & Lou (1990):

$$r^2 \frac{f''}{f} = n(n+1) \tag{34}$$

$$(1 - \mu^2)P'' + a^2 \frac{n+1}{n} P^{1+2/n} + n(n+1)P = 0. \tag{35}$$

There is an arbitrary amplitude of  $P$  in Equation (35) that can be scaled away. Then this ordinary differential Equation (ODE) together with the homogeneous boundary conditions pose an eigenvalue problem to determine the scaled parameter  $a$  as an eigenvalue. Recalling Equation (8), we have the following expression for the nonlinear force-free modes:

$$\mathbf{B} = \frac{-1}{r\sqrt{1-\mu^2}} \left( \frac{\sqrt{1-\mu^2}}{r} \frac{\partial\psi}{\partial\mu} \hat{\mathbf{r}} + \frac{\partial\psi}{\partial r} \hat{\boldsymbol{\theta}} - Q \hat{\boldsymbol{\phi}} \right) \tag{36}$$

where  $\psi = P(\mu)/r^n$  and  $Q = a\psi^{(n+1)/n}$ . Now  $P$  is the solution of Equations (35) and (36) and takes the form

$$\mathbf{B} = \left( \frac{-1}{r^{n+2}} \frac{dP}{d\mu}, \frac{n}{r^{n+2}} \frac{P}{(1-\mu^2)^{1/2}}, \frac{a}{r^{n+2}} \frac{P^{(n+1)/n}}{(1-\mu^2)^{1/2}} \right). \tag{37}$$

Eqn (35) is not straightforward to integrate numerically except for the case  $n = 1$ , which was presented in Low & Lou (1990), because there is an inherent singularity at  $\mu = 0$ . We extend these solutions to higher values of odd  $n$  by using the following transformation:

$$P(\mu) = (1 - \mu^2)^{1/2} F(\mu), \quad (38)$$

through which Equation (37) stands as

$$\mathbf{B} = \left( \frac{-1}{r^{n+2}} \left[ (1 - \mu^2)^{1/2} F'(\mu) - \frac{\mu F(\mu)}{(1 - \mu^2)^{1/2}} \right], \frac{n}{r^{n+2}} F, \frac{a}{r^{n+2}} (1 - \mu^2)^{1/2n} F^{1+1/n} \right) \quad (39)$$

and Equation (35) becomes

$$(1 - \mu^2) F''(\mu) - 2\mu F'(\mu) + \left[ n(n+1) - \frac{1}{(1 - \mu^2)} \right] F(\mu) + a^2 \frac{(n+1)}{n} F^{\frac{(n+2)}{n}} (1 - \mu^2)^{\frac{1}{n}} = 0. \quad (40)$$

Eqn (40) can be solved for all values of positive  $n$ , which represent the physically interesting cases. The initial requirement of  $\psi = P/r^n$  requires only  $n > 0$  where  $n$  can take any positive rational or integral value. A stringent condition on  $n$  is enforced if we demand  $Q = a\psi^{1+1/n}$  is real, which is required for physically acceptable solutions. This means that for rational values of  $n = p/q$ ,  $Q = a\psi\psi^{q/p}$  and  $\psi^q$  should be positive for all even values of  $p$ . Also, this implies that possibilities like (odd  $p$ , odd  $q$ ) and (even  $q$ , odd  $p$ ) are permissible. In summary, solutions exist for all odd values of  $p$ , whereas for even  $p$ , it exists only if  $F(\mu) > 0$  in the domain  $-1 \leq \mu \leq 1$ . As examples, the solutions for  $n = 2/3, 2/5, 4/7$ , etc., are allowed. Therefore the acceptable values of  $n$  form a sufficiently dense set in the range  $0 < n < \infty$ , such that one can find instances of  $p/q$  arbitrarily close to a given  $n$ . Recently, semi analytic solutions to Equation (35) for  $n = 5, 7 \dots 201$  under the assumption of self-similarity were presented in Zhang et al. (2012).

### 5.1. Conditions for Physically Acceptable Solutions

The following conditions are required to be satisfied to obtain physically acceptable solutions:

1. The field should be finite as  $r \rightarrow \infty$ . This is ensured if  $n$  is positive.
2. The field should be well behaved and finite along the axis of symmetry. Because we have

$$B_\theta, B_\phi \propto \frac{1}{(1 - \mu^2)^{1/2}} P(\mu);$$

this requires that  $P(\mu)$  should vanish at  $\mu = 1, -1$ . This gives the condition

$$P(\mu) \rightarrow (1 - \mu^2)^s \quad \text{at} \quad \mu = \pm 1$$

where  $s \geq 1/2$ .

The function  $F(\mu)$  satisfies the boundary condition (see Appendix H)

$$F(\mu) = 0 \quad \text{at} \quad \mu = \pm 1. \quad (41)$$

Further, it follows that Equation (40) reduces to the equation for the associated Legendre polynomials (where the last term is ignorable compared to the third term) in the limit  $\mu^2 \rightarrow 1$ . So we can construct LL solutions by direct integration of Equation (40) subject to Equation (41) for any positive  $n$ . We have cross-verified with the only case,  $n = 1$ , that was given in Low & Lou (1990) and calculated other allowed values of  $n$  as well. The cases for the modes  $n = 1$  to  $n = 3$  are shown in Figure 1 for the first three eigenvalues  $m$  of the variable  $a$ . These solutions are singular at the origin, so the energy and helicity calculations are done excluding a spherical region around the origin. As specific examples of the non integer type, we depict realizations of radial modes  $n = 7/5, 3/2, 9/5$ , in the left column of Figure 5.

## 5.2. Energy and Relative Helicity for the LL Modes

The energy in the magnetic field is given by Equation (B1)

$$E_{\text{ff}}(n, m, r_1) = \frac{1}{4(2n+1)r_1^{2n+1}} \int_{-1}^1 d\mu \left[ P'(\mu)^2 + \frac{n^2 P(\mu)^2}{1-\mu^2} + \frac{a^2 P(\mu)^{(2n+2)/n}}{1-\mu^2} \right] \quad (42)$$

where the expression for the field from Equation (37) is used. The energy of the force-free field calculated using the virial theorem of Equation (B2) gives the equivalent expression

$$E_{\text{ff}} = \frac{1}{4r_1^{2n+1}} \int_{-1}^1 \left\{ \left( \frac{dP}{d\mu} \right)^2 - \frac{(n^2 + a^2 P^{2/n}) P^2}{(1-\mu^2)} \right\} d\mu. \quad (43)$$

The Equation (42) reduces to Equation (43) by the use of Equation (35). It may be noted that the function  $P(\mu)$  is implicitly dependent on the parameters  $n$  and  $m$ . The contour plot in Figure 2 shows the dependence of energy on the variables  $n$  and  $m$  and we find that the magnetic energy of the field increases with both of the variables. The change in energy is very sharp with  $n$  as compared to  $m$ , so the value of contours are given in logarithmic scale. The potential field corresponding to the LL mode is calculated in Appendix C.2, and its final expression is given by

$$\mathbf{B}_P = \left( \sum_{l=0}^{\infty} -(l+1) \frac{b_l}{r^{l+2}} P_l(\mu), \sum_{l=0}^{\infty} \frac{-b_l}{r^{l+2}} (1-\mu^2)^{1/2} \frac{dP_l}{d\mu}, 0 \right), \quad (44)$$

where

$$a_l = 0, \quad b_l = \frac{2l+1}{2(l+1)} r_1^{l-n} \int_{-1}^1 \frac{dP}{d\mu} P_l(\mu) d\mu. \quad (45)$$

The energy for the potential field constructed from the LL modes (see Section C.2) is given by

$$E_{\text{pot}}(l, r_1) = \sum_{l=0}^{\infty} \frac{b_l^2 (l+1)}{2(2l+1) r_1^{2l+1}}. \quad (46)$$

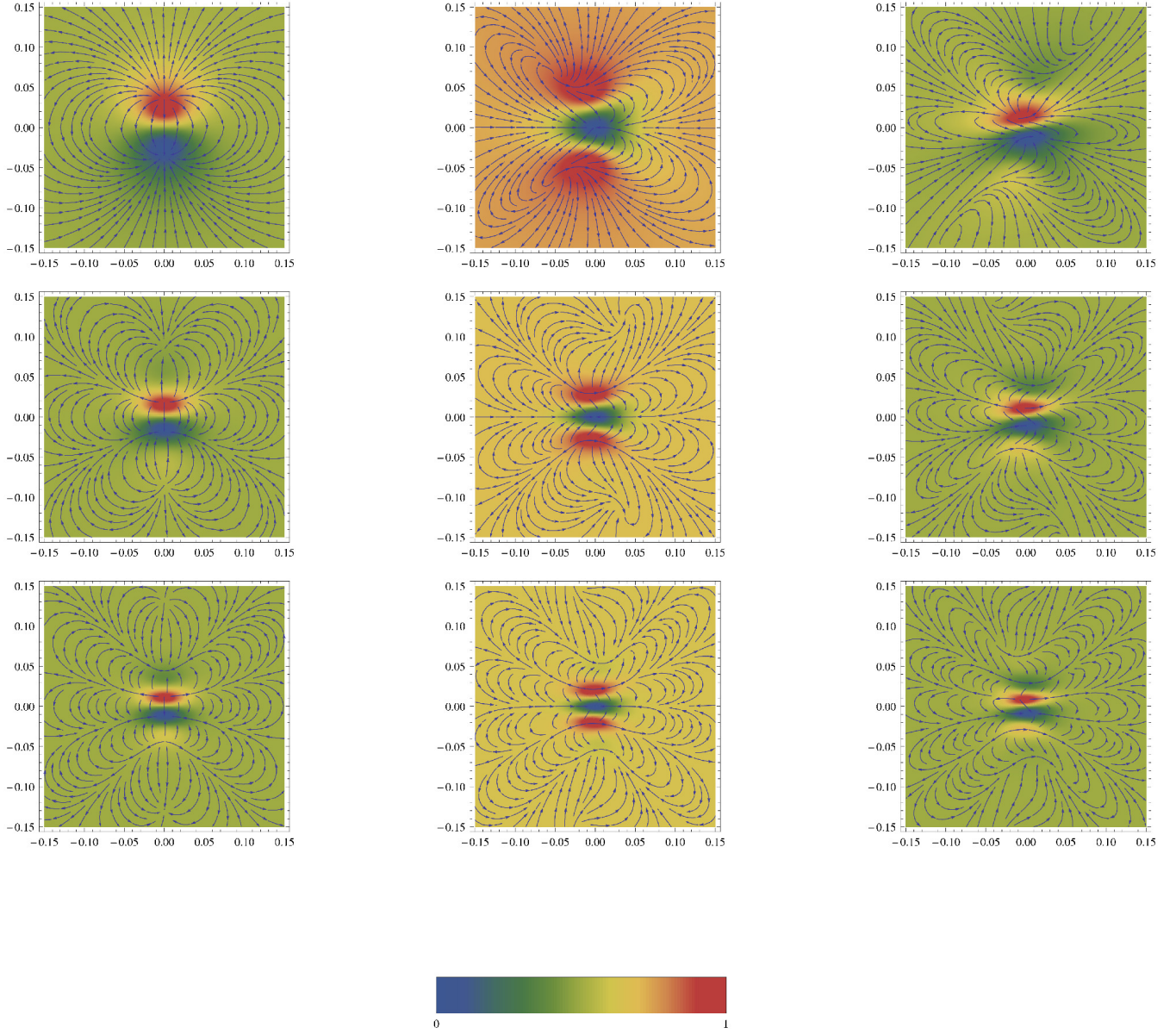


Fig. 1.— Sections (avoiding the origin where the fields are singular) shown are taken perpendicular to the radius at  $r = 0.05$  for different solutions of LL, with angular modes  $m = 1$  to  $m = 3$  (columns) and radial modes  $n = 1$  to  $n = 3$  (rows). The contours represent the magnetic field lines projected on the plane and the density plot represents the strength of the field perpendicular to the plane of the figure. The values 0 and 1 in the color bar correspond to the minimum and maximum values of the perpendicular magnetic field, respectively.

In order to calculate the relative helicity, we find the vector potential for the LL modes in Appendix E given by

$$\mathbf{A} = \left( 0, \frac{-a}{nr^{n+1}} \frac{P(\mu)^{(n+1)/n}}{(1-\mu^2)^{1/2}}, \frac{1}{r^{n+1}} \frac{P(\mu)}{(1-\mu^2)^{1/2}} \right). \quad (47)$$

The vector potential for the potential field is given by Equation (D7) with  $a_l$  and  $b_l$  as defined in Equation (45). Then the relative helicity is calculated from Equation (2) to be

$$H_{\text{rel}}(n, m, r_1) = \int_V (\mathbf{A}_P \cdot \mathbf{B} - \mathbf{A} \cdot \mathbf{B}_P) dV \quad (48)$$

because  $\mathbf{A} \cdot \mathbf{B} = \mathbf{A}_P \cdot \mathbf{B}_P = 0$ . Thus, even if the absolute helicity  $\mathbf{A} \cdot \mathbf{B}$  is zero in our chosen gauge, the cross terms in the Finn–Antonsen formula give rise to the nonzero values of the relative helicity. The expression in Equation (48) can be further simplified to

$$H_{\text{rel}}(n, m, r_1) = -2\pi a \sum_{l=0}^{\infty} \int_{-1}^1 \frac{b_l}{nlr_1^{n+l}} P^{1+1/n} \frac{dP_l}{d\mu} d\mu. \quad (49)$$

Using Equation (6), we get an equivalent form for the relative helicity that works out to be

$$H_{\text{rel}}(n, m, r_1) = \frac{2\pi a}{nr_1^{2n}} \int_{-1}^1 \frac{P^{2+1/n}}{(1-\mu^2)} d\mu. \quad (50)$$

The two formulae in Equations (49) and (50) are equivalent as shown in Appendix F.2.

## 6. SIMULATION OF MAGNETOGRAMS

In this paper, our aim is to get reasonably good and quick estimates of free energy and relative helicity for the active region observed in the magnetograms. It is well known that NLFF fields best represent the solar active regions, and the most useful and widely used analytic solution is the Low–Lou solution in the spherical geometry. Hence this geometry was naturally chosen. In our scheme, we first compute a large set of linear and nonlinear 3D force-free modes in a spherical shell volume where the magnetogram is a tangent plane to the lower boundary, see Figure 3.

For the linear case, the field is defined between radii  $r_0$  and  $r_2$ . A plane representing the magnetogram is placed tangential to a shell of radius  $r_1$ . A potential field is constructed in the spherical shell between radii  $r_1$  and  $r_2$  (region II) using the normal components of the force-free field at the lower boundary,  $r_1$ . For the nonlinear case, the field is defined outside a shell of radius  $r_1$  (region II) where the plane representing the magnetogram is placed tangentially. Again the potential field is constructed using the normal components of the force-free field at  $r_1$ . The fit to the magnetogram data selects a particular mode of force-free field in spherical geometry (details given below). Apart from this, the magnetogram also sets a length scale for the problem and fixes an amplitude of the magnetic field. Both the force-free field and potential field are known completely in region II, so we calculate the free energy and relative helicity (using Finn–Antonesen and Berger



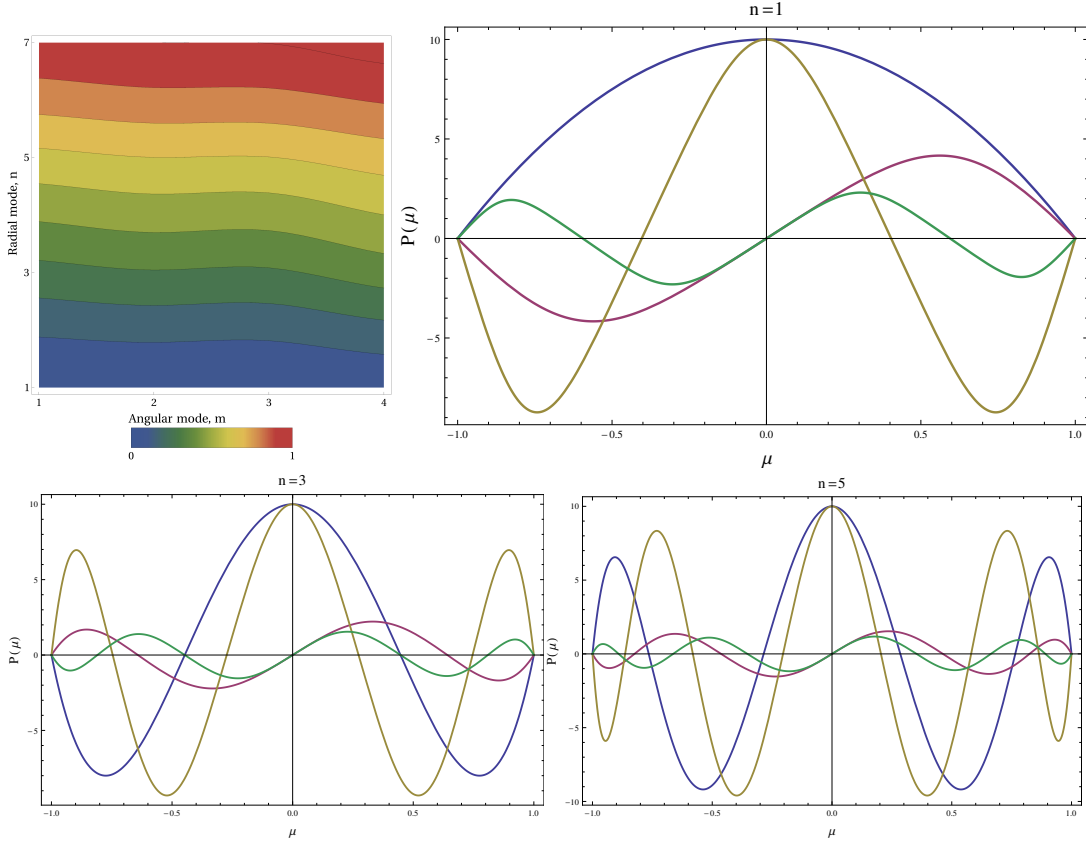


Fig. 2.— Top left panel shows contours of energy for different angular and radial modes for the LL modes. The energies (normalized with respect to the maximum) are shown for different modes at the same lower boundary  $r_1 = 0.5$ . The value of contours are given in logarithmic scale because the parametric dependence is very sharp. The values 0 and 1 in the color bar correspond to the minimum and maximum values of energy, respectively. The next three panels show the realizations of  $P(\mu)$  for the cases of  $m = 1$  to 4 for  $n = 1, 3$  and 5. Note that the number of polarities for a given  $(n, m)$  set is given by  $n + m - 1$ .

formula) in region II. In order to compare with the other estimates available in the literature, where the potential fields are usually extended from the planar surface of the magnetogram to a cuboidal volume over the magnetogram, we rescale our physical quantities obtained for a hemisphere by the factor of the solid angle subtended by the magnetogram at the center. We would like to emphasize that our problem is to reconstruct the entire field from the knowledge of the field in a 2D plane, which does not a priori force any choice of geometry. So calculation of free energy and relative helicity in the shell geometry does not compromise our original goal, which is to get quick reasonable estimates of these quantities over the solid angle subtended by the magnetogram. The validity of this approximation can be seen from the general agreement with other estimates (including observations, presented later in Table 5). An advantage in this method is its ease and

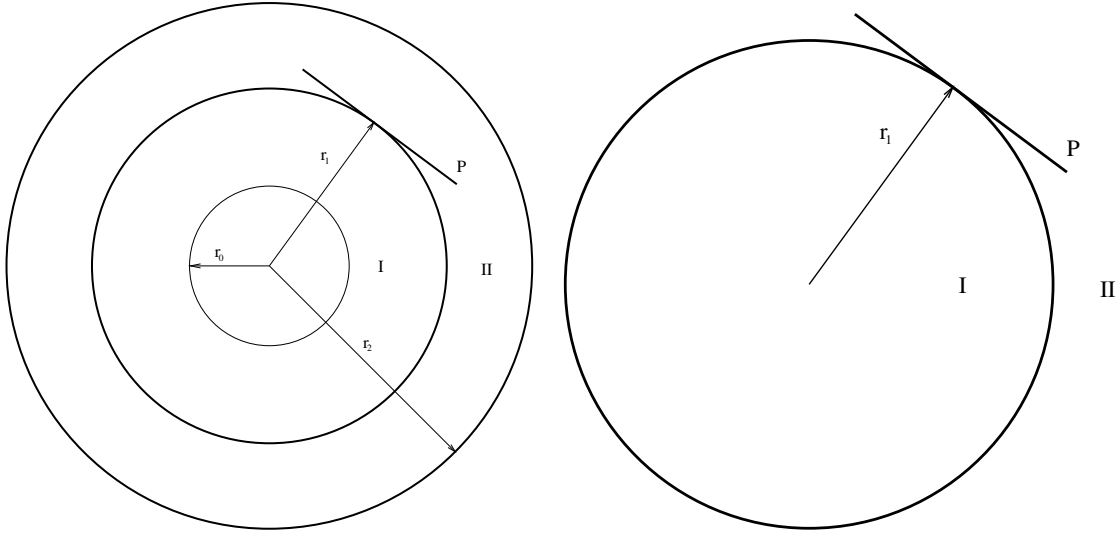


Fig. 3.— Geometry used in the problem for the linear (left panel) and nonlinear (right panel) fields. For the linear case, the field is first computed between radii  $r_0$  and  $r_2$ . A plane representing the magnetogram is placed tangential to a shell of radius  $r_1$ . A potential field is constructed in the spherical shell between radii  $r_1$  and  $r_2$  (region *II*) using the normal components of the force-free field at the lower boundary,  $r_1$ . For the nonlinear case, the field is computed outside a shell of radius  $r_1$  where the plane representing the magnetogram is placed tangentially. Again the potential field is constructed using the normal components of the force-free field at  $r_1$ .

utility in calculating these physical quantities: in particular the relative helicity is thus far not calculated by other approaches. Further, we do not have to assume any other boundary condition for the side walls, as required in the other extrapolation techniques using the cuboidal volume.

We now use the library of LL and C modes by taking 2D sections of the force-free spheres appropriately and compare these sections with the observed magnetograms. We describe the best-fit mode and figure of merit of fit in Section 6.2. The following steps are taken in simulating the sections:

1. We compute the 3D force-free magnetic field in spherical geometry corresponding to a given C and LL mode from Equation (A5) and Equation (37) respectively.
2. The coordinates on the magnetogram are labeled as the  $x$  and  $y$  axes, where the  $x, y \in [-0.5, 0.5]$  so that the magnetogram is of unit length.
3. A cross section of the sphere is taken at a radius  $r_1$ , and all three components of magnetic field are computed over this 2D surface, see Figure 4. The orientation of the magnetogram is given by the three Euler angles  $(\phi', \theta', \psi')$ , of which the angle  $\phi'$  is redundant because the

fields are axisymmetric. The transformation matrix for the Euler rotation is given by

$$\Lambda(\theta', \psi') = \begin{bmatrix} \cos \psi' & \cos \theta' \sin \psi' & \sin \psi' \sin \theta' \\ -\sin \psi' & \cos \theta' \cos \psi' & \cos \psi' \sin \theta' \\ 0 & -\sin \theta' & \cos \theta' \end{bmatrix}. \quad (51)$$

In effect the position and orientation of the section is fixed by three parameters  $(r_1, \theta', \psi')$ . We then transform a point on the magnetogram with coordinates  $(x, y, z)$  by the inverse of  $\Lambda$ .

4. The coordinates in spherical  $\mathbf{x}_S \equiv (r, \theta, \phi)$  are obtained from Cartesian coordinates  $\mathbf{x}_C \equiv (x, y, z)$  through the operator  $S$  given by

$$\begin{aligned} \mathbf{x}_S &= S(\mathbf{x}_C) \\ r &= (x^2 + y^2 + z^2)^{1/2} \\ \phi &= \begin{cases} \arctan(y/x) & x > 0 \\ \arctan(y/x) + \pi & x \leq 0 \end{cases} \\ \theta &= \arccos(z/(x^2 + y^2 + z^2)^{1/2}) \end{aligned}$$

to get  $\mathbf{x}_S$  as a function of  $(x, y, z)$  so that we have the coordinates of all the points on the magnetogram in spherical coordinates

$$\mathbf{x}_S = S(\Lambda^{-1}(\theta', \psi')\mathbf{x}_C). \quad (52)$$

5. We now evaluate the magnetic field in spherical coordinates  $\mathbf{B}_S(\mathbf{x}_S)$  and then convert the components of magnetic field from spherical polar to Cartesian coordinate system so that

$$\mathbf{B}_C[\mathbf{x}_C, \theta', \psi', x, y] = \Lambda(\theta', \psi')T(\mathbf{B}_S[S(\Lambda^{-1}(\theta', \psi')\mathbf{x}_C)]). \quad (53)$$

where

$$T = \begin{bmatrix} \sin \theta \cos \phi & \cos \theta \cos \phi & -\sin \phi \\ \sin \theta \sin \phi & \cos \theta \sin \phi & \cos \phi \\ \cos \theta & -\sin \theta & 0 \end{bmatrix}, \quad (54)$$

is the transformation from spherical to Cartesian. Here the coordinates  $\theta$  and  $\phi$  are locations on the magnetogram computed from Equation (52). Because  $\Lambda$  and  $T$  are orthogonal, their inverses are the corresponding transposes.

We illustrate simulated sections thus generated for the LL modes  $(n, m) = \{(7/5, 2), (3/2, 3), (9/5, 1)\}$  in Figure 5. The parameter values  $(r_1, \theta, \phi)$  chosen are indicated in the caption and the resulting sections are typical of the single- and double-polarity active regions seen in observations.

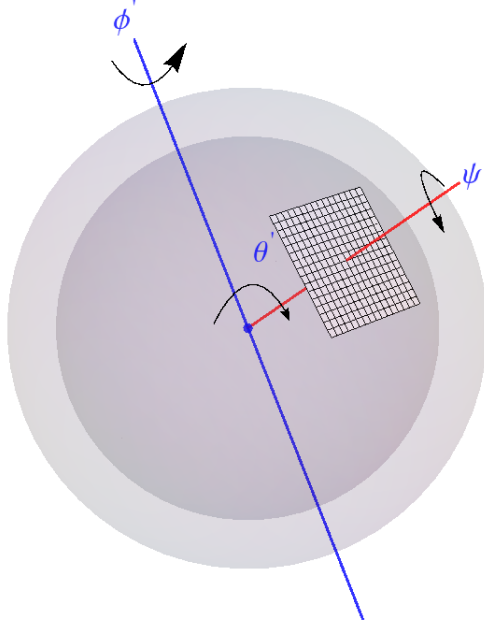


Fig. 4.— Magnetogram is simulated by taking a cross section of the axisymmetric 3D force-free field at a radius  $r_1$ . The magnetogram is then rotated through the Euler angles  $\theta'$  and  $\psi'$  to match the components of the observed magnetogram. The rotation  $\phi'$  is redundant because the field is axisymmetric.

### 6.1. Search Strategy

We have the following free parameters in the problem:

1. The radial and angular mode numbers,  $n$  and  $m$ : the values for  $n$  and  $m$  fix the force-free modes (for both C and LL solutions). Whereas  $n$  takes only integral values for C modes, LL modes can take integral as well as fractional values (with the exceptions mentioned in *Section 5*). The value of  $m$  takes only integers for both C and LL modes.
2. The first derivative  $d = F'(\mu = -1)$ : the value of the derivative of  $F(\mu)$  at the boundary which is used as a boundary condition for solving Equation (40), is a free parameter; this only scales the solution by an arbitrary constant. In this paper we have used  $d = 10$  as a constant input for all calculations.
3. Euler angles,  $\theta'$  and  $\psi'$ : The C modes repeat in  $\theta'$  at an interval of  $\pi/(m+1)$  for a given  $m$  and  $\theta'$  was taken to be the larger of this value and the angle subtended by the magnetogram at the center to avoid redundancy;  $\theta' = \max(\pi/(m+1), \arctan(L/r_1))$ . For LL modes we search in the domain  $\theta' \in [0, \pi]$ . For both cases, we search for  $\psi$  in the range,  $\psi' \in [0, 2\pi]$ . If the magnetogram has  $n_p$  polarities in a range  $\Delta\mu = 1 - \cos\gamma$  for a mode that has  $m_p$  total

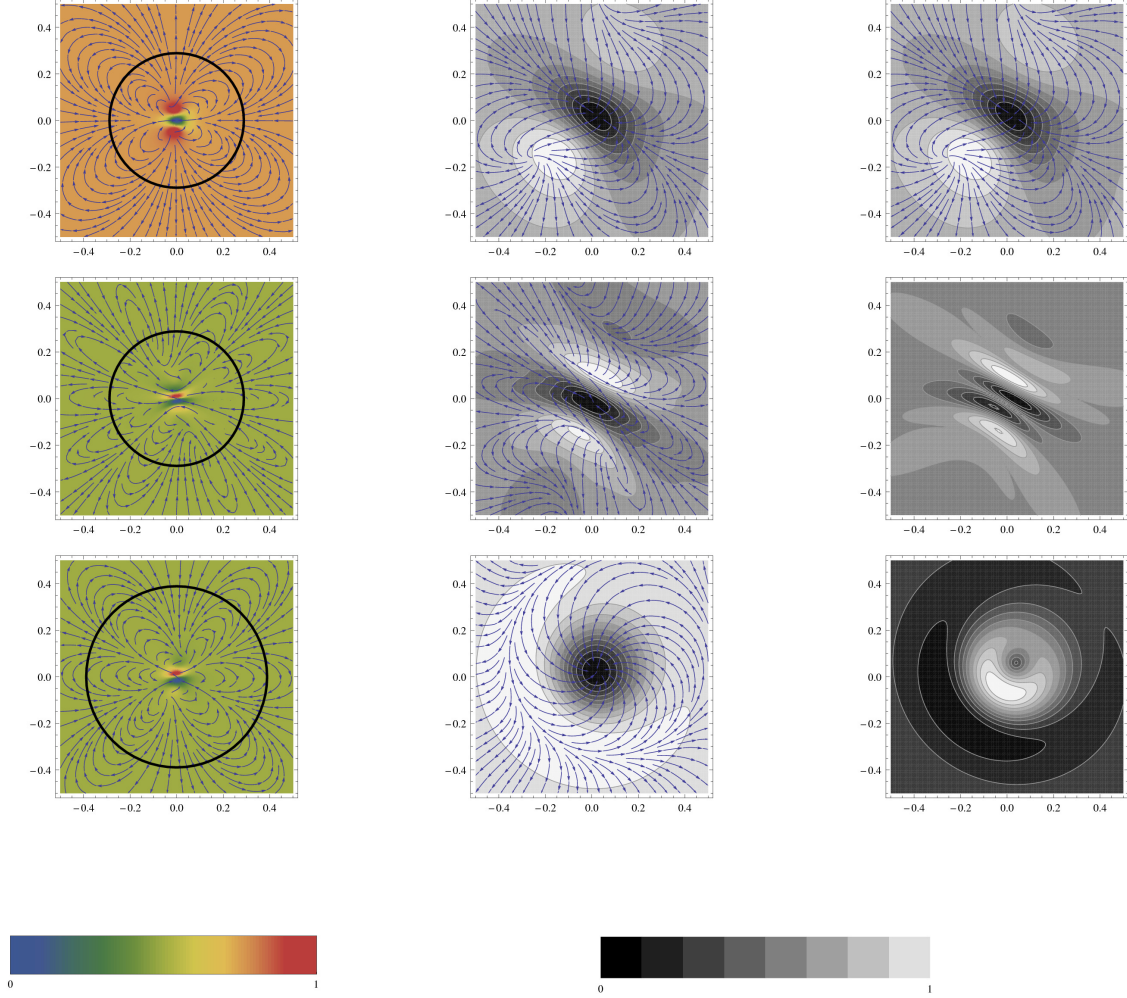


Fig. 5.— Sections for different LL solutions, taken perpendicular to the radius at  $r = 0.05$  with parameters  $(n, m, r_1, \theta, \phi) = \{(7/5, 2, 0.29, 1.75, 4.14), (3/2, 3, 0.29, 1.75, 4.14), (9/5, 1, 0.39, 0.18, 4.14)\}$  are shown in the top, middle and bottom rows respectively. In the left column, the contours represent the magnetic field projected onto the plane of the figure, and the density plot represents the strength of the field perpendicular to it. The circles are drawn at radius  $r_1$ . The middle column is a section of the field and the right column is a section of the resulting current density; for an illustration of the section geometry and the parameters, see Figure 4. The legends representing the strength of component normal to the page are shown below corresponding to the left and middle/right columns. The 0 and 1 in the legend scale correspond to the minimum and maximum values of the normal magnetic field respectively.

polarities over the domain  $[-1, 1]$ , then we estimate

$$\frac{n_p}{m_p} \simeq \frac{\Delta\mu}{2} = \frac{1 - \cos\gamma}{2} = 1/(1 + (r_1/L)^2 4) \quad (55)$$

where  $\gamma$  is the angle subtended by the magnetogram at the center.

4. The radius  $r_1$  at which the cross section is to be taken is in the range 0 to  $r_2$ . Here  $r_2$  is the outer radius up to which the energies and helicity are calculated. In the case of C modes  $r_2$  is finite and necessarily at the root of  $J(m + 3/2, \alpha r)$ . We have restricted the calculations to only one radial oscillation (corresponding to only one visible closed loop along the line of sight), whereas for LL modes  $r_2$  is infinite as the fields tend to zero only at infinity. The finite radial boundary  $r_2$  is needed for the C modes and not the LL modes. For a linear force-free field in the Taylor theory of relaxation in the unbounded atmosphere, the minimum energy state is a C mode provided the domain is finite (Low 1996). In the case of C modes, the constraint that the magnetogram is contained within the sphere of radius  $r_2$  leads to the condition

$$r_1 \leq \sqrt{r_2^2 - L^2/4}. \quad (56)$$

In the case of LL modes, there is no obvious constraint on  $r_1$ .

5. The force-free parameter  $\alpha$ : for C modes,  $\alpha$  is a constant and has to be given as an input. We restrict  $\alpha^{-1}$  to be of order unity in line with typical observed magnetograms where the field reverses over this length.

To summarize, the parameter space to search for C modes is  $(n, m, r_1, r_2, \alpha, \theta', \phi')$ . We start sweeping from the lowest combinations of  $(n, m)$  in increasing energy and searching for  $r_1$  with the constraint on the range of  $\theta'$  and  $r_1$  given above and allowing only for one radial oscillation.

For LL modes, we have to search for the parameters  $(n, m, r_1, \theta', \phi')$ . Here, we start by sweeping from the lowest combinations of  $(n, m)$  and looking for  $r_1$  near unity to find the best-fit lowest energy modes within the allowed range of  $\theta'$  and  $\psi'$ . Due to the computational constraints involved we were only able to survey a subset of the parameter space. The run time for a combination of  $(n, m, \alpha)$  for C modes and  $(n, m)$  for LL modes is about 8 hr of parallel computation on three computers with second generation Intel i7 processors. The search for the best-fit parameter is done in the following manner. For a particular mode of the solution (specified by the values of  $n$ ,  $m$ , and  $\alpha$ , in the case of C modes), we choose six equispaced grid points in the  $\theta'$  and  $\psi'$  domain and eight equispaced points for  $r$ . For the C modes the values for  $r$  are chosen between two Bessel zeros, whereas for the LL modes we start with an initial guess of  $r = 1$ . Then for each combination of  $(r, \theta', \psi')$  the field is computed over a  $380 \times 380$  grid (for a typical magnetogram). Thus, each mode of the solution involves evaluating the field for about 42 million combinations. All of the template grids thus generated are compared with the observed data; following this initial search, the best-fit set is selected and a finer grid of  $(r, \theta', \psi')$  defined about this set with four grid points each is searched to obtain the final parameter set. We plan to expand upon the search in the future when we are able to make our code, which is already parallelized, run on a faster cluster.

## 6.2. Fitting Parameters

In the previous section we described how we explore the parameter space and generate a large ensemble of magnetograms. In order to select the best-fit with the observations, we define a figure of merit,  $c$  for the magnetic field  $\mathbf{B}$  as

$$c = \frac{\langle (\mathbf{B}_T \cdot \mathbf{B}_O) |\mathbf{B}_O| \rangle}{\langle |\mathbf{B}_T|^3 \rangle^{1/3} \langle |\mathbf{B}_O|^3 \rangle^{2/3}},$$

which is the normalized dot product between the observed,  $\mathbf{B}_O$ , and the theoretically simulated field,  $\mathbf{B}_T$ , weighted by the strength of the observed magnetic field so that  $|c|$  would be unity for a perfect correlation. Here  $\langle \rangle$  represents the mean computed over the entire grid. We also calculate the following correlation parameters to estimate the goodness of the fit for the selected configuration

$$d = \frac{\langle (\mathbf{B}_O \cdot \mathbf{B}_T / |\mathbf{B}_T|) \rangle}{\langle |\mathbf{B}_O| \rangle}, \quad \text{and} \quad (57)$$

$$\epsilon = \frac{\langle |\mathbf{B}_T|^2 \rangle}{\langle |\mathbf{B}_O|^2 \rangle}, \quad (58)$$

where  $d$  is the average of the cosine of the angle between the two fields computed over the entire grid, which is normalized by the strength of the observed field, whereas  $\epsilon$  is the ratio of the magnetic energies of the theoretical and observed fields. The amplitude of the theoretical field is set by multiplying a scaling constant,  $g$ , where

$$g^2 = \frac{\langle |\mathbf{B}_O|^3 \rangle / \langle |\mathbf{B}_O| \rangle}{\langle |\mathbf{B}_T|^3 \rangle / \langle |\mathbf{B}_T| \rangle}, \quad (59)$$

which is deduced from the weighted ratio of energies. Because the energy and helicity are computed for the entire sphere, we need to scale down these quantities by the fraction of solid angle subtended by the magnetogram. The fraction of solid angle subtended by a square loop of size  $L$  placed at a distance  $r_1$  from the center is given by

$$\begin{aligned} \Omega_f &= \frac{1}{\pi} \int_0^{L/2} \int_0^{L/2} \frac{r_1 dx dy}{(r_1^2 + x^2 + y^2)^{3/2}} = \frac{1}{\pi} \int_0^{L/2} \frac{dx}{r_1^2 + x^2} \int_0^{L/(2\sqrt{x^2+r_1^2})} \frac{r_1 dz}{(1+z^2)^{3/2}} \\ &= \frac{Lr_1}{2\pi} \int_0^{L/2} \frac{dx}{(r_1^2 + x^2)\sqrt{L^2/4 + r_1^2 + x^2}} = \frac{1}{\pi} \int_0^{\arctan[L/(2r_1)]} \frac{\cos \theta d\theta}{\sqrt{\cos^2 \theta + 4r_1^2/L^2}} \\ &= \frac{1}{\pi} \arcsin \left( \frac{L^2}{L^2 + 4r_1^2} \right). \end{aligned} \quad (60)$$

The final expressions for energy and helicity are given by

$$\overline{E} = E\Omega_f g^2 L^3 \quad \text{and} \quad \overline{H}_{rel} = H_{rel}\Omega_f g^2 L^4, \quad (61)$$

where  $\overline{E}$  and  $\overline{H}_{rel}$  represent the energy and relative helicity, respectively, calculated over the volume containing the magnetogram.

### 6.3. Effectiveness of the Search Strategy

In order to estimate the effectiveness of our search strategy, we try to recover the field configurations and energies of known input fields. The input fields used as test cases are

1. a pure dipole field,
2. an axisymmetric linear force-free field (C modes), and
3. a non axisymmetric linear force-free field, Chandrasekhar & Kendall (1957) (CK modes).

In each of these cases, we gave a 2D cross section of the magnetic field as an input to our code and obtained a best-fit with axisymmetric NLFFs (LL modes). The parameter search grid used for this analysis is the same as that used for the observed field. The details of the fit and the comparison of energy and helicity are presented in Table 1.

No.	Test Field	Mode $n, m$	Correlation, $c$	Energy (input field)	Energy (best-fit field )	Relative Helicity (input field)	Relative Helicity (best-fit field)
a.	Dipole field	1, 1	0.9925	7.77	6.76	0	0
b.	C mode	3, 1	0.662	1.24	1.34	-4.97	0
c.	CK mode	3, 1	0.636	0.237	0.134	-0.327	0

Table 1: The table presents the correlation parameter for fits of the input test field with the LL modes along with a comparison of energy and relative helicity. In all the cases above the length scale of the 2D cross section is taken to be unity.

The summary of our investigations can be presented as follows.

1. *Pure dipole field.* We find that the dipolar field gives an almost exact fit to the LL mode. This is because it is an exact solution to the  $n = 1, m = 1$  LL mode. The accuracy of the fit can be improved by taking more grid points in our parameter space. In this case, the axis of symmetry does not match exactly due to the smaller grid resolution that is chosen because of numerical constraints. Of course when the exact values of the parameters are chosen, we recover perfect fits. We also see that the energy of the best-fit field closely matches that of the original field.
2. *C mode.* We obtain a moderately good fit with 66% correlation with the original field. The  $n = 3, m = 1$  mode is picked up which represents a potential field. This may be suggestive of the fact that the only constant  $\alpha$  solution allowed within the LL modes is the potential  $\alpha = 0$  mode. We find that the energies of the best-fit field match that of the original field within a factor of two.
3. *CK mode.* We get a fit of 64% correlation with the original field. Again in this case the  $n = 3, m = 1$  mode is picked up as in the previous case. The non-axisymmetry of this field makes it more difficult to fit with a axisymmetric NLFF, which accounts for the low correlation.



Thus, we find that we are able to get the correct configuration for the input field (as in the dipole case). . The accuracy of the fits can be improved by taking more grid points in our parameter search space. This is computationally extensive and will be taken up in the near future. We do not get good matches to linear/non axisymmetric linear force-free fields using nonlinear axisymmetric fields where the relative helicity in these cases could not be obtained accurately: the energy however has been obtained in all cases within a factor of two. The morphological matches in all of the three cases are shown in Figure 6. We see that the overall features of fields are well captured in the fits. In this context, we remark that our fits for observed data are higher.

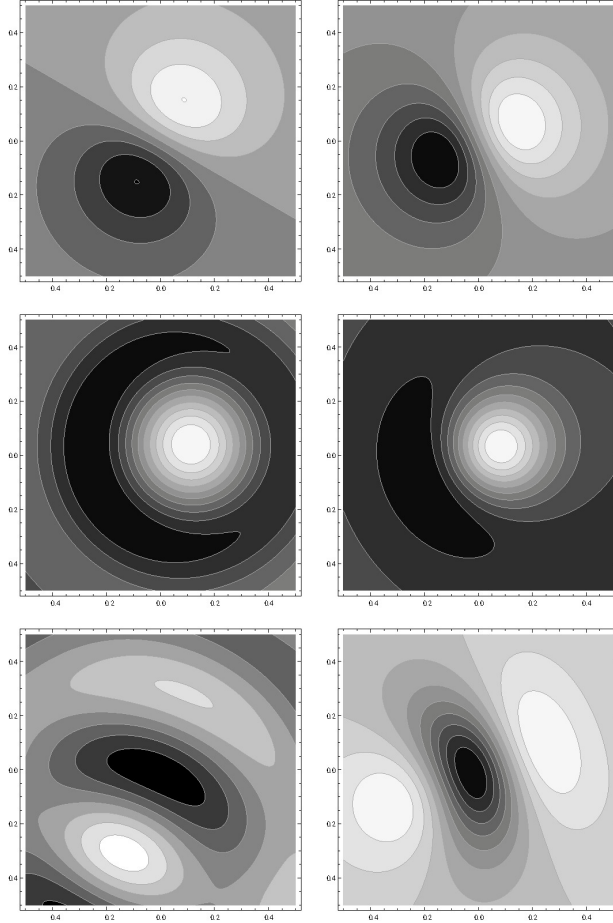


Fig. 6.— Left panels represent the input fields and the right panels represent the corresponding best-fits by LL modes. The input in the top, middle, and bottom rows are dipole, C mode and CK mode, respectively. More details are given in Table 1

## 7. PREPARATION OF OBSERVATIONAL DATA

In order to compare the analytic solutions computed in this paper with the real magnetic field measurements and their associated quantities, we use the active region magnetic field data from the spectropolarimeter (SP) onboard *Hinode*. The (SP) is one of the instruments of the solar optical telescope (SOT). The SOT/SP obtains Stokes profiles with a spatial resolution of  $0.3''$  (Ichimoto et. al. 2008) in magnetically sensitive Fe I lines at 630.15 and 630.25 nm. The SOT/SP can make the map of an active region in four modes, which are normal map, fast map, dynamics and deep magnetogram modes. In this study, we use the data from the fast mode, the spatial resolution along the slit direction is  $0.295''$ , and in the scanning direction it is  $0.317''$  pixel<sup>-1</sup>. The obtained Stokes profiles were calibrated using the solar software suites for the SP. The Stokes vectors have been inverted using the Milne–Eddington inversion (Skumanich & Lites 1987; Lites & Skumanich 1990; Lites et al. 1993), and the three components of magnetic field were obtained. The 180° ambiguity in the transverse field has been resolved using the minimum-energy algorithm developed by Metcalf (1994) and implemented by Leka et al. (2009) in Fortran. This algorithm minimizes the electric current density and divergence simultaneously, selecting the field orientation with minimum free energy. The algorithm is the best among the several codes for automatically resolving the 180° ambiguity (Metcalf et al. 2006). The resulting vector components have been transformed to the disk center (Venkatkrishnan et. al. 1988). The resulting vertical,  $B_z$ , and transverse,  $B_t$ , field strengths have  $1\sigma$  error bars of 8 and 30 G, respectively.

We have chosen magnetograms of three active regions (Table 7) spanning the years 2006 to 2007 for our analysis. Most of the AR appeared in the southern hemisphere at a latitude close to the equator.

No.	Active Region	Date and Time of Obs.	Latitude	Pixel resolution	Length, $L$ ( $10^9$ ) cm
1.	NOAA 10930	2006 Dec 12, 2000 UT	S05	$0.306''$	8.0
2.		2006 Dec 13, 0400 UT		$0.306''$	8.0
3.		2006 Dec 14, 1700 UT		$0.306''$	8.44
4.		2006 Dec 14, 2200 UT		$0.306''$	8.44
5.		2006 Dec 15, 0545 UT		$0.306''$	8.44
6.	NOAA 10923	2006 Nov 11, 1430 UT	S04	$0.306''$	8.44
7.	NOAA 10933	2007 Jan 07, 0000 UT	S05	$0.306''$	8.44

Table 2: Serial numbers are assigned to the active regions in the first column for reference. The date, time and latitude for the observations are given in the next two columns. The last two columns represent the mean pixel resolution and the physical length scale of the magnetogram.

## 8. COMPARISON OF MODELS TO OBSERVATIONS

### 8.1. Results

We list our findings below:

1. All of the field configurations analyzed were found to be negatively twisted as seen from the  $\alpha$  for the C modes and the sign of the helicity for the LL modes. The fits with nonlinear LL modes are substantially better than the linear C modes, confirming the nonlinear nature of the force-free fields.
2. Table 4 lists all of the parameters compiled for the AR listed in Table 7.
3. The AR 10930 has been fit by LL modes with a figure of merit  $c = 0.7$ - $0.8$  and  $d = 0.65$ - $0.7$ . The energy ratio,  $\epsilon$ , is away from unity due to the fact that the data is noisy and that we had not done any preprocessing. There was an X3.4-class flare on 2006 December 13, and we confirm in both models a substantial decrease in free energy and relative helicity after the flare. The relative helicity and free energy in the C mode increased and in the LL mode decreased marginally after the X1.5-class flare on 2006 December 14.
4. The two ARs 10923 and 10933 with single-polarity fitted with potential fields with a high figure of merit  $> 90\%$ . They also show good correlation numbers for  $d$  and  $\epsilon$  (near unity).
5. The formula (55) for the predicted  $m_p(n_p, r_1/L)$  bears out for the force-free configurations found for AR 10930 (see first five rows of Table 8.1 for the modes  $(n, m)$  for C and LL modes). For example, in the case of C modes,  $m_p = 2m - 2 = \{18, 18, 8, 14, 14\}$  for the five cases and we find the estimated  $m_p$  from Equation (55) to be  $\{16, 16, 7.25, 11.7, 11.7\}$ . For the five cases of LL,  $m_p = n + m - 1 = 4$  in all of the five cases, whereas the estimated  $m_p = \{4.25, 4.6, 4.6, 3.8, 3.8\}$  from Equation (55). It is clear that because the  $m_p$  estimates are closer for the LL modes than for the C modes, the corresponding figures of merit are higher for the C modes. The suggested  $m_p$  estimates are for the lowest energy configurations.

### 8.2. Discussion of the Results

AR 10923 and AR 10933 show good fits ( $c > 90\%$ ) with single-polarity potential configurations and are negatively twisted with the energies of  $10.7 \times 10^{33}$  and  $2.063 \times 10^{33}$  erg, respectively. The corresponding goodness of fit parameters ( $d, \epsilon$ ) are near unity and indicate good fits (see Table 4).

Active region NOAA 10930 is a center of focus for several studies and the *Hinode*/SOT has followed the active region for several days in many wavelength regions. The SP produced vector magnetograms of this region until it disappeared on the west limb of the Sun. Using the vector

C Mode Parameters							LL Mode Parameters						
AR No.	Modes $n, m$	$\alpha^{-1}/L$	$r_1/L, r_2/L$ $\theta'/\pi, \psi'/\pi$	$\overline{E}_{ff}$ $10^{33}$ erg	$\overline{E}_{pot}$ $10^{33}$ erg	$\overline{E}_{free}$ $10^{33}$ erg	$\overline{H}_{rel}$ $10^{43}$ $\text{Mx}^2$	Modes $n, m$	$r_1/L$ $\theta'/\pi, \psi'/\pi$	$\overline{E}_{ff}$ $10^{33}$ erg	$\overline{E}_{pot}$ $10^{33}$ erg	$\overline{E}_{free}$ $10^{33}$ erg	$\overline{H}_{rel}$ $10^{43}$ $\text{Mx}^2$
1.	1, 10	-0.09	1.32, 1.45 0.034, 1.142	1.50	0.905	0.595	-1.91	3, 2	0.53 0.117, 1.37	3.46	2.77	0.69	-0.322
2.	2, 10	-0.091	1.34, 1.85 -0.04, 0.095	6.27	0.760	5.51	-10.69	3, 2	0.57 0.67, 0.45	11.69	9.34	2.35	-1.17
3.	1, 5	-0.094	0.81, 0.99 -0.02, 0.38	2.71	1.18	1.53	-4.96	3, 2	0.57 0.167, 1.37	5.21	4.16	1.05	-0.552
4.	1, 8	-0.089	1.10, 1.24 0.015, 1.25	1.633	0.928	0.705	-2.30	3,2	0.67 0.117, 1.29	4.41	3.52	0.89	-5.49
5.	1, 8	-0.089	1.10, 1.24 0.015, 1.25	1.54	0.877	0.663	-2.18	3, 2	0.67 0.117, 1.29	4.16	3.32	0.84	-0.518
6.	1, 0	-0.461	1.65, 2.07 -0.97, 0.75	119.4	90.5	28.9	-535.3	1, 1	0.43 0.83, 1.33	10.70	10.70	0.0	0.0
7.	1, 0	-0.75	2.95, 3.37 -1.0, -0.15	178.1	161.1	17	-530.2	3, 1	0.57 $3.18 \times 10^{-7}$ , 1.67	2.063	2.063	0.0	0.0

Table 3: The table contains the correlations of the simulated and observed magnetograms for their best-fit with C and LL modes with the corresponding parameters and the estimations of the free energy and relative helicity. Details of the different active regions for each row are given in the corresponding rows in Table 7. The numbers  $(n, m)$  refer to the radial and angular modes, and  $\alpha$  is the proportionality constant between **B** and **J**, which is scaled with respect to  $L$ , the length scale of the magnetogram. The inner radius is represented by  $r_1$  where the magnetogram is placed and  $r_2$  is the outer radius of the computation region. In the case of C modes,  $r_2$  is finite because we have restricted the calculations to only one radial oscillation, whereas for LL modes,  $r_2$  is infinite because the fields tend to zero only at infinity. The Euler angles through which the magnetogram is rotated are represented by  $\theta'$  and  $\psi'$ .  $\overline{E}_{ff}$ ,  $\overline{E}_{pot}$ ,  $\overline{E}_{free}$  and  $\overline{H}_{rel}$  are the normalized force-free energy, potential energy, free energy and the relative helicity of the magnetic field configuration, respectively.

C Mode					LL Mode		
N0.	AR No.	$c$	$d$	$\epsilon$	$c$	$d$	$\epsilon$
1.	NOAA 10930	0.58	0.521	1.834	0.81	0.695	1.273
2.		0.581	0.511	1.876	0.70	0.645	1.88
3.		0.33	0.324	1.791	0.75	0.673	1.687
4.		0.42	0.395	1.724	0.76	0.698	1.765
5.		0.40	0.374	1.644	0.74	0.697	1.682
6.	NOAA 10923	0.76	0.888	1.517	0.92	0.928	0.943
7.	NOAA 10933	0.56	0.788	2.40	0.95	0.871	1.113

Table 4: The correlation parameters obtained for estimating the goodness of fit for different active regions. The definitions of the correlation parameters are given in Section 6.2.

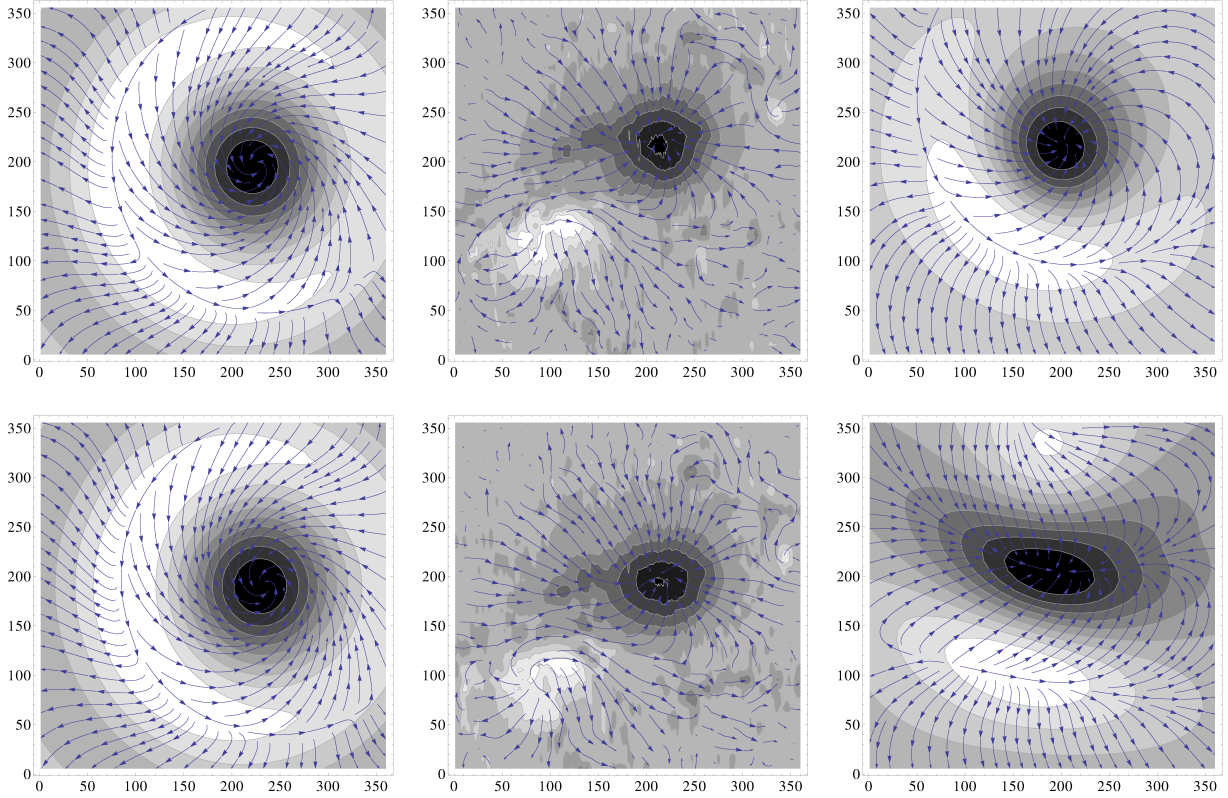


Fig. 7.— Magnetograms for active region NOAA 10930 are shown in the top and bottom panels of the figure for the dates 2006 December 12 and 13, respectively. The left and right panels represent the magnetograms simulated by the C and LL modes, respectively. The middle panel represents the magnetogram observation by *Hinode*. There was an occurrence of an X 3.4-class flare between the dates; the figure depicts the field configuration before and after the flare.

magnetic field measurements at the photospheric levels and by applying a technique called pre-processing several authors employ NLFF extrapolation methods to compute the coronal magnetic fields (e.g., Schrijver et al. 2008). An X3.4-class flare has occurred in this active region on 2006 December 13. Using the 3D magnetic fields information, Schrijver et al. (2008) found  $3 \times 10^{32}$  ergs of drop in free energy after the flare compared to the preflare free energy. On the other hand, Guo et al. (2008) find that only  $2.4 \times 10^{31}$  erg of energy were released during the flare. At the same time, using a similar technique, Jing et al. (2010) did not find any release in free energy during the flare; instead they found a slight increase in free energy after the flare. He et al. (2011) also estimate the free energy for three time series vector magnetograms of the same solar active region, NOAA 10930 through NLFFF extrapolation which were observed in a 26 hour period from 2006 December 10-11. They note a rise in the free energy of the system from  $1.25\text{--}1.42 \times 10^{33}$  erg. These results are summarized in Table 5 along with our results.

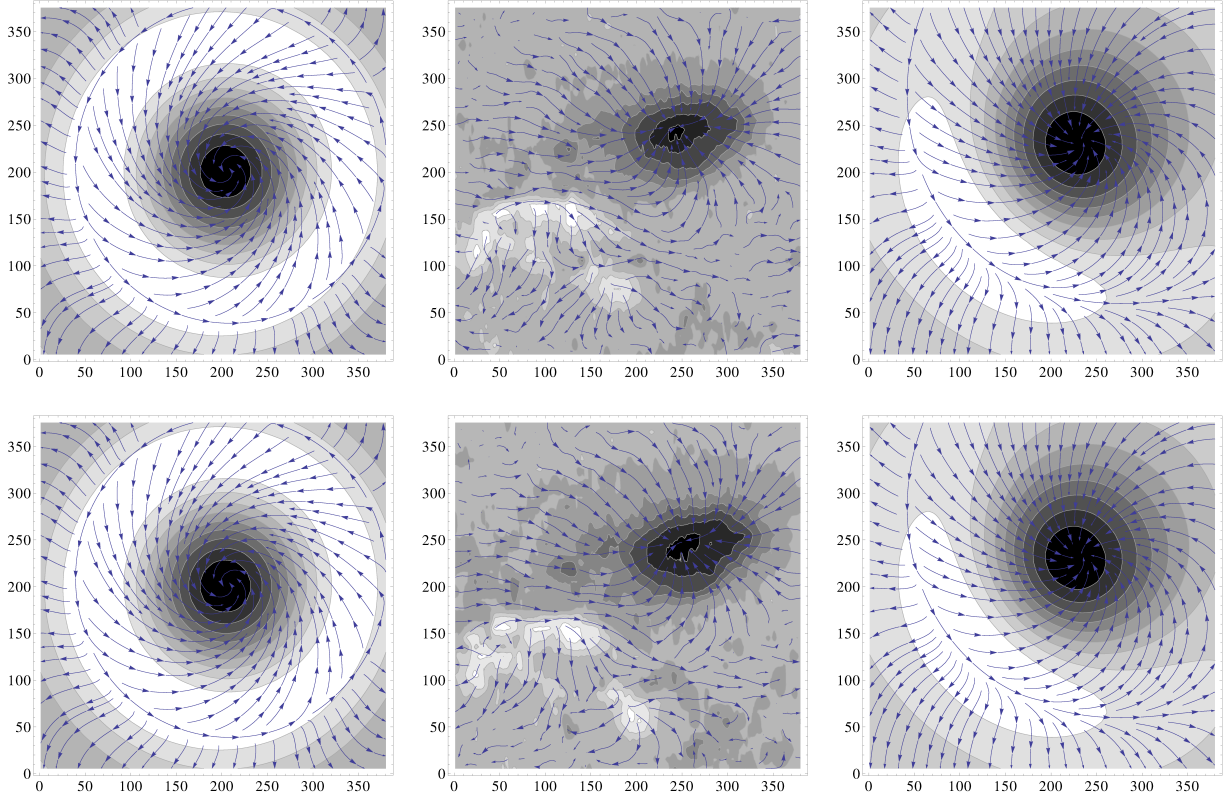


Fig. 8.— Magnetograms for active region NOAA 10930 are shown in the top and bottom panels of the figure for the dates 2006 December 14 and 15, respectively. The left and right panels represent the magnetograms simulated by the C and LL modes, respectively. The middle panel represents the magnetogram observation by *Hinode*. There was an occurrence of an X-1.5 class flare between the dates; the figure depicts the field configuration before and after the flare.

We were able to get good correlations for this region for both C (40-60 %) and LL (70-80%) modes; see Figures 7 & 8 and Table 4. We find that free energies derived from the LL model are consistent with a drop after both of the flare events (note that the time coverage before and after the flare is not complete), indicating a strong probability of a peak in the free energy (and relative helicity) just before the first flare event, see Figure 9. This picture is conducive to the idea that the loss of the free energy in the photosphere is strongly related to the energy dissipated in the flare events.

The coronal mass ejection (CME) associated with this event carried kinetic energy (deprojected velocity ) of  $4.5 \times 10^{32}$  erg with it (Ravindra & Howard 2010). This is in rough agreement with our estimate of a loss of  $1.66 \times 10^{33}$  erg (LL modes) because about half of this would be released in the kinetic energy channel. The magnetic cloud associated with the CME had a helicity of about  $-7 \times 10^{41}$  Mx<sup>2</sup> as estimated here by Ravindra et al. (2011) which is much less than the drop in

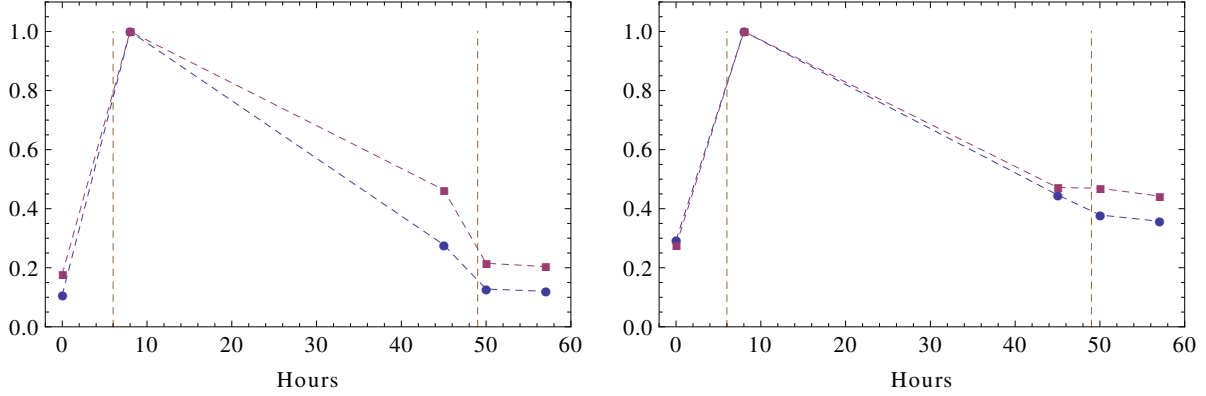


Fig. 9.— Free energy (circle) and relative magnetic helicity (square) simulated for AR 10930 (see rows 1-5 in Table 8.1) for the C (left) and LL (right) modes, plotted as a function of time. The time of the first observation (2006 December 12; UT 2000) is set as 0 hr. The vertical lines represent the times of X3.4- and X1.3-class flares, respectively. The values on the y-axis have been normalized with respect to their maximum.

Model <sup>ref</sup>	Pre-flare					Post-flare					$\Delta \bar{E}_{free}$	$\Delta \bar{H}_{rel}$
	$\bar{E}_{ff}$ $10^{33}$ erg	$\bar{E}_{pot}$ $10^{33}$ erg	$\bar{E}_{ff}/\bar{E}_{pot}$	$\bar{E}_{free}$ $10^{33}$ erg	$\bar{H}_{rel}$ $10^{43}$ $\text{Mx}^2$	$\bar{E}_{ff}$ $10^{33}$ erg	$\bar{E}_{pot}$ $10^{33}$ erg	$\bar{E}_{ff}/\bar{E}_{pot}$	$\bar{E}_{free}$ $10^{33}$ erg	$\bar{H}_{rel}$ $10^{43}$ $\text{Mx}^2$	$10^{33}$ erg	$10^{43}$ $\text{Mx}^2$
C modes <sup>a</sup>	1.5	0.905	1.66	0.595	-1.91	6.27	0.76	8.25	5.51	-10.69	4.915	-8.78
LL modes <sup>a</sup>	3.46	2.77	1.249	0.69	-0.322	11.69	9.34	1.252	2.35	-1.17	1.66	-0.848
Current-field iteration <sup>b</sup>	...	...	1.32	...	...	...	...	1.14	...	...	-.32	...
Optimization <sup>c</sup>	1.33	1.2	1.13	1.11	...	1.27	1.16	.11	1.09	...	-.02	...
Weighted optimization <sup>d</sup>	...	...	...	~.75	...	...	...	...	~.85	...	.1	...

Table 5: The values for the energy of the force-free field and the corresponding potential field for the active region NOAA 10930 mentioned in literature are compiled in the table along with our results for reference. The quantities such as the free energy of the configuration, ratio between energies of the force-free and potential field and the change in free energy before and after the flare are also mentioned. a: current paper, b: Schrijver et. al. (2008), c: Guo et. al. (2008), d: Jing et. al. (2010)

helicity estimated for the LL modes to be  $-0.322 \times 10^{43} \text{ Mx}^2$ . However our estimate of the relative helicity injected into the active region corona is found to be  $-0.848 \times 10^{43} \text{ Mx}^2$  before the initiation of an X3.4-class flare which is comparable to the  $-4.3 \times 10^{43} \text{ Mx}^2$  found by Park et al. (2010). All of the NLFF extrapolation techniques employed (other than in this work) in computing the free energy using the vector magnetic field data made use of preprocessing technique to make the field closer to force-free. However, in doing so the field gets smoothed thereby reducing the field strength and hence the free energy.



For the same data sets other authors using different NLFF extrapolation techniques for the analysis obtain slightly different results. In some cases, there is an increase in the free energy after the flare, whereas in other cases they find that it decreases. In our analysis, both the free energy and relative helicity increase after the first flare, as can be seen from the last two columns in Table 5. The ratio of the energies of the force-free field and the potential field remains almost constant before and after the flare for the LL mode, whereas for the C mode it increases. This can be used to infer that during the flare process there is a dynamic evolution of both the force-free field and the potential field from a lower to higher energy state, implying that there was a peak in free energy and relative helicity between the two observations which are separated by a large time gap of 8 hr.

## 9. SUMMARY AND CONCLUSIONS

Here we first summarize the key results of this paper.

### 1. *Analytic Results.*

We have shown that there are two solutions possible (albeit known already and denoted here as C and LL) from the separability assumption. We calculate the energies and relative helicity of the allowed force-free fields in a shell geometry. The final expression for the field of C modes is given in Equation (A5). We then calculated the corresponding potential field for calculating relative helicity in this region. The expressions for the potential field and its vector potential are given in Equations (A6) and (29). The relative helicity thus calculated is given by Equation (30). The expression for energies of the force-free field and the potential field are given by Equations (26) and (28), respectively whereby we can calculate the free energy of the system using Equation (1). The alternative expressions for the energy of the force-free field and relative helicity are given in Equations (27) and (31), respectively which are analytically in agreement with the previous expressions.

For the LL mode we were able to extend the solution set obtained in Low & Lou (1990) from  $n = 1$  to all rational values of  $n = \frac{p}{q}$  by solving the Equation (40) for all cases of odd  $p$  and for cases of  $q > p$  for even  $p$ , in effect extending solution to practically all  $n$ . The final expression for the magnetic field is given by Equation (39) and its vector potential by Equation (47). The expression for the potential field consistent with this force-free field is given by Equation (44) and the corresponding vector potential is given by Equation (29) with the constants evaluated from Equation (45). The relative helicity in the region using the Finn–Antonsen formula is given by Equation (49). The energies for the force-free and potential fields are given by Equations (42) and (46), respectively. Again, the alternative expressions for the energy of the force-free field and relative helicity are given in Equations (43) and (50), respectively which are analytically in agreement with the previous expressions. For convenience these results are included in the formularies for C and LL modes in Table 6.

C MODES	
$\mathbf{B}(r_1 < r < r_2) = \left( \frac{-J_{m+3/2}(\alpha r)}{r^{3/2}} \frac{d}{d\mu} [(1-\mu^2)C_m^{3/2}(\mu)], \frac{-1}{r} \frac{d}{dr} [r^{1/2}J_{m+3/2}(\alpha r)](1-\mu^2)^{1/2}C_m^{3/2}(\mu), \frac{\alpha J_{m+3/2}(\alpha r)}{r^{1/2}}(1-\mu^2)^{1/2}C_m^{3/2}(\mu) \right)$	
$\mathbf{A}(r_1 < r < r_2) = \mathbf{B}/\alpha; \quad a_{m+1} = \frac{(m+2)r_1^{m+3/2}J_{m+3/2}(\alpha r_1)}{r_1^{2m+3}-r_2^{2m+3}}; \quad b_{m+1} = \frac{(m+1)r_2^{2m+3}r_1^{m+3/2}J_{m+3/2}(\alpha r_1)}{r_1^{2m+3}-r_2^{2m+3}}$	
$\mathbf{B}_P(r_1 < r < r_2) = \left( \left[ (m+1)a_{m+1}r^m - \frac{(m+2)b_{m+1}}{r^{m+3}} \right] P_{m+1}(\mu), -(1-\mu^2)^{1/2} \left[ a_{m+1}r^m + \frac{b_{m+1}}{r^{m+3}} \right] \frac{dP_{m+1}}{d\mu}, 0 \right)$	
$\mathbf{A}_P(r_1 < r < r_2) = \left( 0, 0, (1-\mu^2)^{1/2}P'_l(\mu) \left[ \frac{a_l r^l}{l+1} - \frac{b_l}{l r^{l+1}} \right] \right)$	
$E_v(r) = \frac{(m+1)(m+2)}{2(2m+3)} \left[ r \left[ \frac{d}{dr} \{ r^{1/2} J_{m+3/2}(\alpha r) \} \right]^2 + \{ \alpha^2 r^2 - (m+1)(m+2) \} J_{m+3/2}^2(\alpha r) \right];$	
$E_{\text{ff}}(\alpha, n, m, r_1, r_2) = E_v(r_2) - E_v(r_1) = \frac{(m+1)(m+2)}{2(2m+3)} \left[ 2 \int_{r_1}^{r_2} \alpha^2 r J_{m+3/2}^2(\alpha r) dr - r_1^{1/2} J_{m+3/2}(\alpha r_1) \frac{d}{dr} \{ r^{1/2} J_{m+3/2}(\alpha r) \} \Big _{r=r_1} \right]$	
$E_{\text{pot}}(m, r_1, r_2) = \frac{1}{2(2m+3)} \int_{r_1}^{r_2} \left[ \left( (m+1)a_{m+1}r^{m+1} - \frac{(m+2)b_{m+1}}{r^{m+2}} \right)^2 + (m+1)(m+2) \left( a_{m+1}r^{m+1} + \frac{b_{m+1}}{r^{m+2}} \right)^2 \right] dr$	
$H_{\text{rel}}^{FA}(\alpha, n, m, r_1, r_2) = \frac{8\pi E_{\text{ff}}}{\alpha} + \frac{4\pi(m+1)(m+2)}{\alpha(2m+3)} \left[ \alpha^2 \int_{r_1}^{r_2} \left( \frac{a_{m+1}r^{m+1}}{m+2} - \frac{b_{m+1}}{(m+1)r^{m+2}} \right) r^{3/2} J_{m+3/2}(\alpha r) dr \right. \\ \left. + r_1^{1/2} \left( a_{m+1}r_1^{m+1} + \frac{b_{m+1}}{r_1^{m+2}} \right) J_{m+3/2}(\alpha r_1) \right]$	
$H_{\text{rel}}^B(\alpha, n, m, r_1, r_2) = \frac{8\pi\alpha(m+1)(m+2)}{2m+3} \int_{r_1}^{r_2} r J_{m+3/2}^2(\alpha r) dr.$	
LL MODES	
$\mathbf{B}(r < r_2) = \left( \frac{-1}{r^{n+2}} \frac{dP}{d\mu}, \frac{n}{r^{n+2}} \frac{P}{(1-\mu^2)^{1/2}}, \frac{a}{r^{n+2}} \frac{P^{(n+1)/n}}{(1-\mu^2)^{1/2}} \right); \quad \mathbf{A}(r < r_2) = \left( 0, \frac{-a}{nr^{n+1}} \frac{P(\mu)^{(n+1)/n}}{(1-\mu^2)^{1/2}}, \frac{1}{r^{n+1}} \frac{P(\mu)}{(1-\mu^2)^{1/2}} \right)$	
$a_l = 0, \quad b_l = \frac{2l+1}{2(l+1)} r_1^{l-n} \int_{-1}^1 \frac{dP}{d\mu} P_l(\mu) d\mu; \quad \mathbf{B}_P(r_1 < r < r_2) = \left( \sum_{l=0}^{\infty} -(l+1) \frac{b_l}{r^{l+2}} P_l(\mu), \sum_{l=0}^{\infty} \frac{-b_l}{r^{l+2}} (1-\mu^2)^{1/2} \frac{dP_l}{d\mu}, 0 \right).$	
$\mathbf{A}_P(r_1 < r < r_2) = \left( 0, 0, (1-\mu^2)^{1/2} P'_l(\mu) \left[ \frac{a_l r^l}{l+1} - \frac{b_l}{l r^{l+1}} \right] \right); \quad E_{\text{pot}}(l, r_1) = \sum_{l=0}^{\infty} \frac{b_l^2(l+1)}{2(2l+1)r_1^{2l+1}}$	
$E_{\text{ff}}(n, m, r_1) = \frac{1}{4(2n+1)r_1^{2n+1}} \int_{-1}^1 d\mu \left[ P'(\mu)^2 + \frac{n^2 P(\mu)^2}{1-\mu^2} + \frac{a^2 P(\mu)^{(2n+2)/n}}{1-\mu^2} \right] = \frac{1}{4r_1^{2n+1}} \int_{-1}^1 \left\{ \left( \frac{dP}{d\mu} \right)^2 - \frac{(n^2 + a^2 P^{2/n}) P^2}{(1-\mu^2)} \right\} d\mu$	
$H_{\text{rel}}^{FA}(n, m, r_1) = -2\pi a \sum_{l=0}^{\infty} \int_{-1}^1 \frac{b_l}{nlr_1^{n+l}} P^{1+1/n} \frac{dP_l}{d\mu} d\mu = H_{\text{rel}}^B(n, m, r_1) = \frac{2\pi a}{nr_1^{2n}} \int_{-1}^1 \frac{P^{2+1/n}}{(1-\mu^2)} d\mu.$	

Table 6: Formulary for the various quantities calculated for the C and LL modes.  $\mathbf{B}$  and  $\mathbf{A}$  denote the force-free magnetic field and its corresponding vector potential. The same quantities for the potential field are denoted by  $\mathbf{B}_P$  and  $\mathbf{A}_P$  respectively.  $E_{\text{ff}}$ ,  $E_{\text{pot}}$ ,  $E_{\text{free}}$  and  $H_{\text{rel}}$  are the force-free energy, potential energy, free energy and the relative helicity of the magnetic field configuration respectively calculated using the Finn Antonesen & Berger formulae that are analytically equivalent.

## 2. Numerical Results.

We formulated a search strategy with parameters including two Euler rotations of the force-free sphere and a variable set that corresponds to the various C and LL modes; see Section 6. A study of effectiveness of our search strategy is presented in Section 6.3. Here we find that we are able to get the correct configuration for the input field (as in the dipole case) and are able to fit the energies within a factor of two. We then studied the field configurations for three active regions, (Table 7) and calculated the free energy and relative helicity for these cases. We were able to get reasonable fits for the above cases; see Table 4. All of the field configurations analyzed were found to be negatively twisted as seen from the  $\alpha$  for the C modes and the helicity of the LL modes; see Table 8.1. The fits with nonlinear LL modes seem to be better than the linear C modes. In the case of AR 10930, there was an X3.4-class flare on 2006 December 13, and we confirm in both modes a substantial decrease in free energy and relative helicity after the flare. A comparison of results obtained in this paper with those in the literature for the same flare event is presented in Table 5. The relative helicity and free energy in the C mode increased and in the LL mode decreased marginally after the X1.5-class flare on 2006 December 14. The two ARs 10923 and 10933 with single-polarity show very high correlation ( $> 90\%$ ) with potential fields. We were not able to explore the full parameter space because of the computational constraints mentioned in Section 6. Because our best-fit with the observational data for the LL modes is substantially better ( $75\%$ ) than those obtained in the test cases, this lends much credibility to the results presented in the paper.

We find that the approach taken here is fairly good in estimating the quantities of interest, namely relative helicity and free energy; see Table 5 and Section 8. In order to compare with the other estimates available in the literature, where the potential fields are usually extended from the planar surface of the magnetogram to a cuboidal volume over the magnetogram, we rescale our physical quantities obtained for a hemisphere by the factor of the solid angle subtended by the magnetogram at the center. This enables us to approximate their trend before and after a flare event. The validity of this approximation can be seen from the general agreement with other estimates (including observations). An advantage in this method is its ease and utility in calculating these physical quantities, in particular the relative helicity is thus far not calculated by other approaches. Further, we don't have to assume any other boundary conditions for the side walls, as required in the other extrapolation techniques using the cuboidal volume. This method can also provide a useful reconstruction of the NLFFs as well as reasonable input field for other numerical techniques. It is clear that nonlinear LL modes are dominantly better fits than the linear C modes. The search is now limited by computational constraints; in the future, we hope to improve the fits by applying the method to a larger space of geometrical parameters and in more cases of mode numbers  $n$  and  $m$ .

The LL solutions of  $n = 1$  in Low & Lou (1990) and  $n = 5, 7, 9$  (odd cases) in Flyer et al. (2004) have been extended here to the cases of nearly all  $n$ . The topological properties of these extended

solutions can be further studied by considering other boundary conditions. The analytic solutions for LL suffer from the problem of a singularity at the origin, which render them unphysical; this implies that more realistic boundary conditions are necessary.

To learn more about the evolution and genesis of these structures, it would be useful to carry out dynamical simulations that allow for footpoint motions with the analytic input fields constructed above to study how the nonlinearity develops; a stability analysis of the nonlinear modes would also be a useful tool (Berger (1985) has analyzed the linear constant  $\alpha$  case). Clearly, these are difficult mathematical problems to be addressed in the future.

The authors thank the referee for the valuable, constructive and insightful comments. The authors would like to acknowledge the *Hinode* team for the photospheric magnetogram data. *Hinode* is a Japanese mission developed and launched by ISAS/JAXA, with NAOJ as domestic partner and NASA and STFC (UK) as international partners. It is operated by these agencies in cooperation with ESA and NSC (Norway). We would also like to acknowledge IIA for providing the computational facilities and Sandra Rajiva for editorial support. A.P. would like to thank CSIR for the SPM fellowship.

## A. BOUNDARY CONDITIONS AND FORMULAE FOR C MODE FIELDS

The conditions to be satisfied at a interface (where  $\alpha$  has a discontinuity) are

1. The divergence condition implies the continuity of the normal component of the magnetic field, whereas the absence of surface currents on the boundaries leads to continuity of the parallel components of the field. Therefore magnetic field  $\mathbf{B}$  should be continuous.
2. The normal component of the current density  $\mathbf{J}$  should be continuous because there is no accumulation of charges at the boundary.

The second condition requires the continuity of the normal component of  $\alpha\mathbf{B}$ ; in contrast, the first condition requires the normal component of  $\mathbf{B}$  to be continuous. If  $\alpha$  changes discontinuously at a spherical shell (say at a radius  $\mathcal{R}$ ), then the two conditions can be met only if the normal component of  $\mathbf{B}$  vanishes. In spherical coordinates, the boundary conditions at the shell are therefore,  $B_r = 0$ ,  $[B_\theta] = 0$  and  $[B_\phi] = 0$ . This condition on  $B_r$  at  $r = \mathcal{R}$  can be met only if

$$g_{m+3/2}(\alpha r)|_{r=\mathcal{R}} = 0. \quad (\text{A1})$$

Let

$$g_{m+3/2}(\alpha r) = c_1 J_{m+3/2}(\alpha r) + c_2 Y_{m+3/2}(\alpha r) \quad (\text{A2})$$

where  $c_1$  and  $c_2$  are constants to be determined from the boundary conditions. Finiteness of  $g$  at  $r = 0$  demands  $c_2 = 0$ ; physically this implies that the poloidal flux, is finite. Then

$$g_{m+3/2}(\alpha r) = c_1 J_{m+3/2}(\alpha r). \quad (\text{A3})$$

Finally, the expression for magnetic field is given by

$$\mathbf{B} = \left( -\frac{1}{r^2} \frac{\partial}{\partial \mu} [S_m r^2 (1 - \mu^2)], \frac{-1}{r \sqrt{(1 - \mu^2)}} \frac{\partial}{\partial r} [S_m r^2 (1 - \mu^2)], \alpha r \sqrt{(1 - \mu^2)} S_m \right). \quad (\text{A4})$$

The above expression can be further simplified by substituting for  $S_m$  using Equations (20) and (A3) to

$$\begin{aligned} \mathbf{B} = & \left( \frac{-J_{m+3/2}(\alpha r)}{r^{3/2}} \frac{d}{d\mu} [(1 - \mu^2) C_m^{3/2}(\mu)], \right. \\ & \left. \frac{-1}{r} \frac{d}{dr} [r^{1/2} J_{m+3/2}(\alpha r)] (1 - \mu^2)^{1/2} C_m^{3/2}(\mu), \frac{\alpha J_{m+3/2}(\alpha r)}{r^{1/2}} (1 - \mu^2)^{1/2} C_m^{3/2}(\mu) \right). \end{aligned} \quad (\text{A5})$$

The various modes of C modes are shown in Figure 10 for different values of the variable  $m$ . Note that  $m$  represents the number of angular oscillations of the mode. The total number of poles in the sphere are  $2m$ . The self-similarity of the solutions is evident from Figure 10.

The derivation for the potential field corresponding to Equation (A5) is given in Appendix C. The final expression for the potential field is found to be

$$\mathbf{B}_P = \left( \left[ (m+1) a_{m+1} r^m - \frac{(m+2) b_{m+1}}{r^{m+3}} \right] P_{m+1}(\mu), -(1 - \mu^2)^{1/2} \left[ a_{m+1} r^m + \frac{b_{m+1}}{r^{m+3}} \right] \frac{dP_{m+1}}{d\mu}, 0 \right), \quad (\text{A6})$$

where  $P_{(m+1)}(\mu)$  are the Legendre polynomials, and where the coefficients are given as

$$\chi_l = \chi_{m+1}(r_1) = \frac{(m+1)(m+2)}{r_1^{3/2}} J(m+3/2, \alpha r_1) \quad (\text{A7})$$

$$\begin{aligned} a_l = a_{m+1} &= \frac{\chi_{m+1}(r_1)}{(m+1)} \frac{r_1^{m+3}}{r_1^{2m+3} - r_2^{2m+3}} \\ b_l = b_{m+1} &= \frac{(m+1)}{(m+2)} a_{m+1} r_2^{(2m+3)} \end{aligned} \quad (\text{A8})$$

The above expressions can be further simplified by substituting for  $\chi_l$ , which gives

$$a_{m+1} = \frac{(m+2) r_1^{m+3/2} J_{m+3/2}(\alpha r_1)}{r_1^{2m+3} - r_2^{2m+3}}; \quad b_{m+1} = \frac{(m+1) r_2^{2m+3} r_1^{m+3/2} J_{m+3/2}(\alpha r_1)}{r_1^{2m+3} - r_2^{2m+3}} \quad (\text{A9})$$

## B. ENERGY FOR CLOSED FIELD LINES OF C MODE

The energy of a force-free magnetic field in a spherical shell geometry is given by

$$E(\mathbf{B}) = \frac{1}{8\pi} \int_{r_1}^{r_2} \int_{-1}^1 \int_0^{2\pi} |\mathbf{B}|^2 r^2 dr d\mu d\phi = \frac{1}{4} \int_{r_1}^{r_2} \int_{-1}^1 |\mathbf{B}|^2 r^2 dr d\mu, \quad (\text{B1})$$

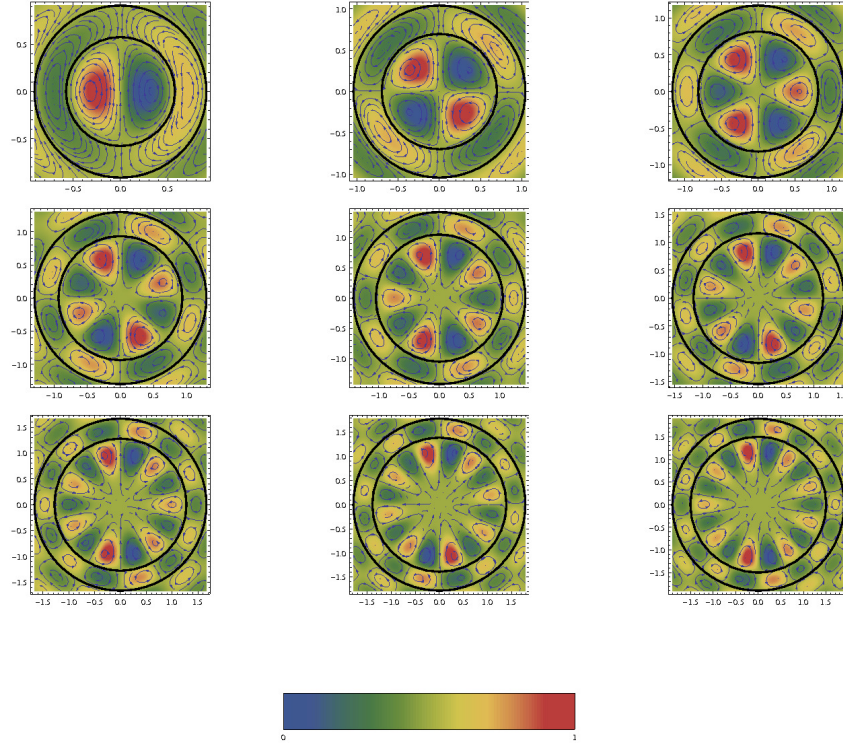


Fig. 10.— Different angular modes from  $m = 1$  (top left) to  $m = 9$  (bottom right) are shown. The contours represent the poloidal stream function  $\psi$  and the density plot represents the strength of the azimuthal field  $B_\phi$ . The two circles are drawn at first and second radial roots. The 0 and 1 in the legend corresponds to the minimum and maximum values of  $B_\phi$ , respectively.

where axisymmetry is applied in the last step. The expression for energy for the force-free field given in Equation (B1) uses a volume integral, whereas we can calculate it via a surface integral using the virial theorem for force-free fields (Chandrasekhar 1961) in spherical geometry as

$$E_{\text{ff}} = \frac{1}{8\pi} \int_V |\mathbf{B}|^2 dV = \frac{1}{8\pi} \int_S |\mathbf{B}|^2 \mathbf{r} \cdot d\mathbf{S} - \frac{1}{4\pi} \int_S (\mathbf{B} \cdot \mathbf{r})(\mathbf{B} \cdot d\mathbf{S}) \quad (\text{B2})$$

where  $S$  is the surface enclosing the volume of interest  $V$ . In axisymmetry, the Equation (B2) reduces to

$$E_{\text{ff}} = \frac{1}{8\pi} \int_V |\mathbf{B}|^2 dV = \frac{\mathcal{R}^3}{4} \int_{-1}^1 (B_\theta^2 + B_\phi^2 - B_r^2) d\mu. \quad (\text{B3})$$

where  $\mathcal{R}$  is the radius of the shell. For the energy of a potential field, we use  $E_P = E(\mathbf{B}_P)$ , which is calculated from Equation (B1). In order to study the dependence of energy on the various radial

and angular modes, we first calculate the contribution from the toroidal component given by

$$E_T(\alpha, n, m, r_1, r_2) = \frac{1}{4}\alpha^2 \int_{r_1}^{r_2} dr r J_{m+3/2}^2(\alpha r) \int_{-1}^1 d\mu (1 - \mu^2) \left[ C_m^{3/2}(\mu) \right]^2. \quad (\text{B4})$$

using Equation (B1) and  $E(\mathbf{B}) = E(\mathbf{B}_T) + E(\mathbf{B}_P)$ ; the total energy (for volumes containing closed-field lines) is given by  $E_{\text{ff}} = 2E_T$  (Chandrasekhar 1961). The energy for C mode can be calculated analytically if the field lines close at the inner and outer boundaries. The radial part of the integration in Equation (B4) can be written as

$$R = \alpha^2 \int_{r_1}^{r_2} dr r J_{m+3/2}^2(\alpha r). \quad (\text{B5})$$

If  $r_1 = 0$  and  $r_2 = r_{nm}$ , where  $Z_{nm} = \alpha r_{nm}$  is the  $n$ th root of  $J_{m+3/2}(\alpha r)$ , then Equation (B5) can be written as

$$R = \frac{1}{2}(Z_{nm})^2 \left[ J_{m+5/2}(Z_{nm}) \right]^2. \quad (\text{B6})$$

The angular part of Equation (B4) can be written as

$$\Theta = \int_{-1}^1 d\mu (1 - \mu^2) C_m^{3/2}(\mu)^2. \quad (\text{B7})$$

Using the orthogonality properties of Gegenbauer polynomials, the above integral can be evaluated as

$$\Theta = \frac{\pi \Gamma(m+3)}{4!(m+3/2)[\Gamma(3/2)]^2} = \frac{2(m+1)(m+2)}{2m+3}. \quad (\text{B8})$$

Combining Equations (B6) and (B8), we obtain the following expression for Equation (B4)

$$E_T = \frac{Z_{nm}^2}{4} \frac{(m+1)(m+2)}{2m+3} \left[ J_{m+5/2}(Z_{nm}) \right]^2. \quad (\text{B9})$$

and plot contours of the result in Figure 11 (left panel). We find that for a sphere of fixed radius, the energy increases with higher angular  $m$  and radial  $n$  modes. The radial modes of the solution are given by the Bessel functions, which represent the number of radial oscillations and the energy of the field increases with the number of oscillations. The angular modes are given by  $(1 - \mu)^{1/2} C_m^{3/2}(\mu)$ , which are presented in the right panel of Figure 11, and the field reverses  $(m+1)$  times for a given value of  $m$ .

### C. MATCHING POTENTIAL FIELDS TO FORCE-FREE FIELDS AT THE INNER SHELL

A potential field is defined by the equation

$$\nabla \times \mathbf{B}_P = 0. \quad (\text{C1})$$

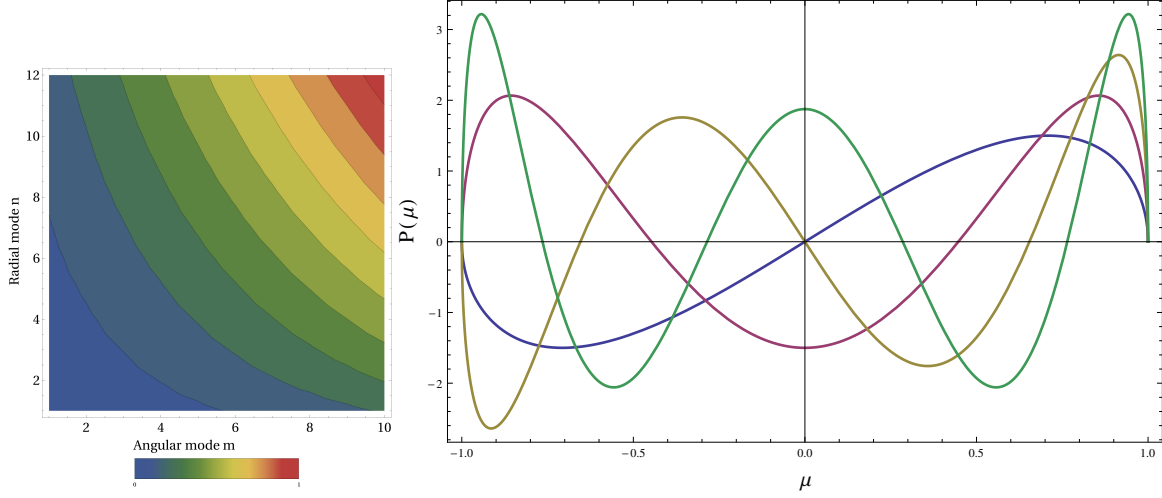


Fig. 11.— Left panel shows contours of energy for different angular and radial modes for C modes computed for the same volume and normalized with respect to the maximum. The 0 and 1 in the legend refer to the maximum and minimum values of the energies respectively. The right panel shows the behavior of  $P(\mu)$ , which changes sign  $(m + 1)$  times in the domain for a given value of  $m$ .

Thus the field can be expressed as  $\mathbf{B}_P = \nabla \Phi_P$  for a scalar potential  $\Phi_P$  which satisfies the Laplace equation  $\nabla^2 \Phi_P = 0$ . The general solution for this equation in spherical coordinates is given by

$$\Phi_P(r, \mu) = \sum_{l=0}^{\infty} \left( a_l r^l + \frac{b_l}{r^{l+1}} \right) P_l(\mu) \quad (\text{C2})$$

where  $P_l(\mu)$  is the Legendre polynomial of order  $l$ ;  $a_l$  and  $b_l$  are constant coefficients to be determined by matching the normal components of potential field with that of the force-free field at the boundaries. We have to solve the Laplace equation for a spherical shell with  $r_1$  and  $r_2$  as inner and outer boundaries.

The radial component of the potential field  $[B_r(r, \mu)]_P$  is given by

$$[B_r(r, \mu)]_P = (\nabla \Phi)_r = \frac{\partial \Phi}{\partial r} = \sum_{l=0}^{\infty} P_l(\mu) \chi_l(r) \quad (\text{C3})$$

where  $\chi_l$  is given by

$$\chi_l(r) = \left[ l a_l r^{l-1} - (l + 1) \frac{b_l}{r^{l+2}} \right]. \quad (\text{C4})$$

We assume that the radial component of the force-free magnetic field can be separated as functions of  $r$  and  $\mu$  denoted by  $R(r)$  and  $\Theta(\mu)$ , respectively:

$$[B_r(r, \mu)]_{ff} = R(r) \Theta(\mu). \quad (\text{C5})$$



To match the radial components of potential and force-free fields, we use equations (C3) and (C5) and equate the two fields at the lower boundary,  $r = r_1$ :

$$R(r_1)\Theta(\mu) = \sum_{l=0}^{\infty} P_l(\mu)\chi_l(r_1). \quad (\text{C6})$$

Using the orthogonality property of Legendre functions we get

$$R(r_1) \int_{-1}^1 \Theta(\mu) P_l(\mu) d\mu = \frac{2}{(2l+1)} \chi_l(r_1). \quad (\text{C7})$$

So, the expansion coefficients for the potential field can be obtained from Equation (C7) as

$$\chi_l(r_1) = \frac{(2l+1)}{2} R(r_1) \int_{-1}^1 \Theta(\mu) P_l(\mu) d\mu \quad (\text{C8})$$

### C.1. Matching Potential Field to C Modes at the Inner Shell

Using Equations (C8) and (A3) we can write at the inner boundary  $r = r_1$

$$\chi_l(r_1) = \frac{-(2l+1)}{2r_1^{3/2}} J(m+3/2, \alpha r_1) \int_{-1}^1 \frac{\partial}{\partial \mu} \left[ C_m^{3/2}(\mu)(1-\mu^2) \right] P_l(\mu) d\mu \quad (\text{C9})$$

$$= \frac{(m+1)(m+2)}{r_1^{3/2}} J(m+3/2, \alpha r_1), \quad (\text{C10})$$

where  $l = m+1$ ; the calculation of the  $\mu$  integral in Equation (C9) is given in appendix section G. At the outer boundary at  $r = r_2$ , we have  $\chi_l(r_2) = 0$ , which results in the following condition for the coefficients  $a_l$  and  $b_l$

$$b_l = b_{(m+1)} = \frac{(m+1)}{(m+2)} a_{(m+1)} r_2^{(2m+3)}. \quad (\text{C11})$$

Using Equation (C4) and the above equation, we find the following expression for the coefficient  $a_{(m+1)}$

$$a_l = a_{(m+1)} = \frac{\chi_{(m+1)}(r_1)}{(m+1)} \frac{r_1^{(m+3)}}{r_1^{(2m+3)} - r_2^{(2m+3)}}. \quad (\text{C12})$$

Upon simplification the coefficients can be written as

$$a_{m+1} = \frac{(m+2)r_1^{m+3/2} J_{m+3/2}(\alpha r_1)}{r_1^{2m+3} - r_2^{2m+3}}; \quad b_{m+1} = \frac{(m+1)r_2^{2m+3} r_1^{m+3/2} J_{m+3/2}(\alpha r_1)}{r_1^{2m+3} - r_2^{2m+3}} \quad (\text{C13})$$

Thus the expression for the potential field is given by

$$\mathbf{B}_P = \left( \left[ (m+1)a_{(m+1)}r^m - \frac{(m+2)b_{(m+1)}}{r^{(m+3)}} \right] P_{(m+1)}(\mu), -(1-\mu^2)^{1/2} \left[ a_{(m+1)}r^m + \frac{b_{(m+1)}}{r^{(m+3)}} \right] \frac{dP_{(m+1)}}{d\mu}, 0 \right). \quad (\text{C14})$$

### C.2. Matching Potential Field to LL Modes at the Inner Shell

We recall the definitions for the general potential field from Equation (C2). Now the boundary condition at the outer boundary  $r_2(=\infty)$  is given by  $\chi_l(r_2) = 0$ , and because the potential should be finite for all values of  $r$ , it implies that

$$a_l = 0 \quad (\text{C15})$$

and the scalar potential takes the form

$$\Phi_P(r, \mu) = \sum_{l=0}^{\infty} \frac{b_l}{r^{l+1}} P_l(\mu) \quad (\text{C16})$$

whereas the radial component of the potential field is given by

$$B_r(r, \mu) = \sum_{l=0}^{\infty} -(l+1) \frac{b_l}{r^{l+2}} P_l(\mu). \quad (\text{C17})$$

From Equation (36) we recall that the radial component of the nonlinear field has the following form

$$B_r(r, \mu) = -\frac{1}{r^{n+2}} \frac{dP}{d\mu}. \quad (\text{C18})$$

Equating the two radial fields at the lower boundary,  $r = r_1$  we get

$$\sum_{l=0}^{\infty} -(l+1) \frac{b_l}{r_1^{l+2}} P_l(\mu) = -\frac{1}{r_1^{n+2}} \frac{dP}{d\mu}. \quad (\text{C19})$$

Using the orthogonality property of the Legendre polynomials we get the following expression for the expansion coefficient  $b_l$ :

$$b_l = \frac{2l+1}{2(l+1)} r_1^{l-n} \int_{-1}^1 \frac{dP}{d\mu} P_l(\mu) d\mu. \quad (\text{C20})$$

So the final expression for the potential field matched to LL modes is given by

$$\mathbf{B}_P = \left( \sum_{l=0}^{\infty} -(l+1) \frac{b_l}{r^{l+2}} P_l(\mu), \sum_{l=0}^{\infty} \frac{-b_l}{r^{l+2}} (1-\mu^2)^{1/2} \frac{dP_l}{d\mu}, 0 \right). \quad (\text{C21})$$

### D. VECTOR POTENTIAL OF POTENTIAL FIELDS

The vector potential for the potential field is given by the relation

$$\nabla \times \mathbf{A}_P = \nabla \Phi_P, \quad (\text{D1})$$

where  $\Phi_P$  is the scalar potential obtained from Equation (C2). Because a potential field is entirely poloidal and the curl of a toroidal field is always poloidal, we expect  $\mathbf{A}_P$  to have only toroidal components. Then an axisymmetric field  $\mathbf{A}_P$  will be of the following form:

$$\mathbf{A}_P = A_\phi(r, \mu) \hat{\phi} \quad (\text{D2})$$

Expanding the above equation in spherical polar coordinates, we obtain the following pair of equations

$$\frac{-1}{r} \frac{\partial}{\partial \mu} \left[ (1 - \mu^2)^{1/2} A_\phi \right] = \frac{\partial \Phi_P}{\partial r} \quad (\text{D3})$$

$$\frac{1}{r} \frac{\partial}{\partial r} (r A_\phi) = \frac{(1 - \mu^2)^{1/2}}{r} \frac{\partial \Phi_P}{\partial \mu} \quad (\text{D4})$$

Solving the above two equations simultaneously, we find the unique solution

$$A_\phi(r, \mu) = \sum_{l=0}^{\infty} (1 - \mu^2)^{1/2} P'_l(\mu) \left[ \frac{a_l r^l}{l+1} - \frac{b_l}{l r^{l+1}} \right]. \quad (\text{D5})$$

$$A_\phi(r, \mu) = \sum_{l=0}^{\infty} (1 - \mu^2)^{1/2} P'_l(\mu) \left[ \frac{a_l r^l}{l+1} - \frac{b_l}{l r^{l+1}} \right]. \quad (\text{D6})$$

So, the final expression is given by

$$\mathbf{A}_P = \sum_{l=0}^{\infty} \left( 0, 0, (1 - \mu^2)^{1/2} P'_l(\mu) \left[ \frac{a_l r^l}{l+1} - \frac{b_l}{l r^{l+1}} \right] \right). \quad (\text{D7})$$

## E. VECTOR POTENTIAL FOR LL MODES

Because  $\mathbf{A}$  is uncertain within a choice of gauge, we choose a convenient gauge such that the radial component of the vector potential,  $A_r$  is zero. Then the vector potential in spherical polar coordinates can be written as

$$\mathbf{A} = (0, A_\theta, A_\phi). \quad (\text{E1})$$

Using the definition  $\mathbf{B} = \nabla \times \mathbf{A}$ , we get the following three equations for the components of  $\mathbf{A}$

$$\begin{aligned} \frac{-1}{r^2} \frac{\partial \psi}{\partial \mu} &= \frac{-1}{r} \frac{\partial}{\partial \mu} \left[ (1 - \mu^2)^{1/2} A_\phi \right] \\ \frac{-1}{r(1 - \mu^2)^{1/2}} \frac{\partial \psi}{\partial r} &= \frac{-1}{r} \frac{\partial}{\partial r} (r A_\phi) \\ \frac{a \psi^{(n+1)/n}}{(1 - \mu^2)^{1/2}} &= \frac{\partial (r A_\theta)}{\partial r}. \end{aligned} \quad (\text{E2})$$

By solving the above set of equations, we find

$$\mathbf{A} = \left( 0, \frac{-a}{n r^{n+1}} \frac{P(\mu)^{(n+1)/n}}{(1 - \mu^2)^{1/2}}, \frac{1}{r^{n+1}} \frac{P(\mu)}{(1 - \mu^2)^{1/2}} \right) \quad (\text{E3})$$

As a consequence of equations (36, E3),  $\mathbf{A} \cdot \mathbf{B} = 0$  everywhere. For closed-field lines in a volume, the magnetic helicity

$$H = \int \mathbf{A} \cdot \mathbf{B} dV = 0. \quad (\text{E4})$$

## F. EQUIVALENCE OF FINN ANTONSEN AND BERGER FORMULAE FOR FORCE-FREE SPHERES

### F.1. C Modes

To show the equivalence of expressions of relative helicity obtained from Equations (30) and (31), we first express Equation (30) as

$$H_r = \frac{8\pi E_{\text{ff}}}{\alpha} + \frac{4\pi(m+1)(m+2)}{\alpha(2m+3)}(I_1 + I_2) \quad (\text{F1})$$

where  $E_{\text{ff}}$  is given by Equation (26) and  $I_1$  is the integral given by

$$I_1 = \int_{r_1}^{r_2} \alpha^2 \left( \frac{a_{m+1}r^{m+1}}{m+2} - \frac{b_{m+1}}{(m+1)r^{m+2}} \right) r^{3/2} J_{m+3/2}(\alpha r) \quad (\text{F2})$$

and  $I_2$  is the boundary term given by

$$I_2 = r_1^{1/2} \left( a_{m+1}r_1^{m+1} + \frac{b_{m+1}}{r_1^{m+2}} \right) J_{m+3/2}(\alpha r_1). \quad (\text{F3})$$

Upon simplification, we get

$$I_1 + I_2 = \left( \frac{a_{m+1}r_1^{m+2}}{m+2} - \frac{b_{m+1}}{(m+1)r_1^{m+1}} \right) \frac{d}{dr} \left[ r^{1/2} J_{m+3/2}(\alpha r) \right] \Big|_{r=r_1}. \quad (\text{F4})$$

Now from the continuity of the radial component of the force-free field to the potential field at  $r = r_1$ ,  $(\mathbf{B}_P)_r = (\mathbf{B})_r$ , where  $\mathbf{B}$  and  $\mathbf{B}_P$  are given by Equations (A5) and (A6) respectively, we find

$$\left( \frac{a_{m+1}r_1^{m+2}}{m+2} - \frac{b_{m+1}}{(m+1)r_1^{m+1}} \right) = r_1^{1/2} J_{m+3/2}(\alpha r_1) \quad (\text{F5})$$

which leads to

$$I_1 + I_2 = r_1^{1/2} J_{m+3/2}(\alpha r_1) \frac{d}{dr} \left[ r^{1/2} J_{m+3/2}(\alpha r) \right] \Big|_{r=r_1}. \quad (\text{F6})$$

Substituting Equations (26) and (F6) in Equation (F1) we arrive at Equation (31).

### F.2. LL Modes

To prove the equivalence of the expressions of relative helicity given in Equations (49 & 50), we start with Equation (C19), which can be rewritten as

$$\sum_{l=0}^{\infty} (l+1) \frac{b_l}{r_1^l} P_l(\mu) = \frac{1}{r_1^n} \frac{dP}{d\mu}. \quad (\text{F7})$$

Integrating the above equation with respect to  $\mu$  and rearranging the terms, we get

$$\sum_{l=0}^{\infty} (l+1) \frac{b_l}{r_1^{l-n}} \int P_l(\mu) d\mu = P. \quad (\text{F8})$$

Now from the Legendre differential equation, we have the identity

$$\left[ (1-\mu^2) \frac{dP_l}{d\mu} \right] = -l(l+1) \int P_l d\mu. \quad (\text{F9})$$

Substituting Equation (F9) in Equation (F8), we get

$$-\sum_{l=0}^{\infty} \frac{b_l}{lr_1^{l-n}} \left[ (1-\mu^2) \frac{dP_l}{d\mu} \right] = P. \quad (\text{F10})$$

Multiplying both sides of Equation (F10) by  $\frac{2\pi a P^{1+1/n}}{nr_1^{2n}(1-\mu^2)}$ , we get the equality between the integrands of Equations (49) and (50).

## G. CALCULATION OF ANGULAR INTEGRAL IN THE EXPRESSION (C9)

Here we give the derivation of the angular integral in Equation (C9):

$$\int_{-1}^1 \frac{\partial}{\partial \mu} \left[ C_m^{3/2}(\mu)(1-\mu^2) \right] P_l(\mu) d\mu. \quad (\text{G1})$$

We now expand Gegenbauer polynomials in terms of Legendre polynomials by using the following relation:

$$(1-\mu^2)C_m^{3/2}(\mu) = (1+m) [P_m(\mu) - \mu P_{m+1}(\mu)] = (1-\mu^2)P'_{m+1}(\mu). \quad (\text{G2})$$

Equation (G1) can now be written as

$$\begin{aligned} & \int_{-1}^1 \frac{\partial}{\partial \mu} \left[ (1-\mu^2)P'_{m+1}(\mu) \right] P_l(\mu) d\mu \\ &= \left[ P_l(\mu)(1-\mu^2)P'_{m+1}(\mu) \right]_{-1}^1 - \int_{-1}^1 P'_l(\mu)P'_{m+1}(\mu)(1-\mu^2) d\mu \\ &= \int_{-1}^1 P'_l(\mu) d\mu \int (m+1)(m+2)P_{m+1}(\mu) d\mu \\ &= \left[ \int (m+1)(m+2)P_{m+1}(\mu) P_l(\mu) d\mu \right]_{-1}^1 - \int (m+1)(m+2)P_{m+1}(\mu)P_l(\mu) d\mu \\ &= -(m+1)(m+2)\delta_{0,m+1}P_l(\mu) - \frac{2(m+1)(m+2)}{2l+1}\delta_{l,m+1} \\ &= -\frac{2(m+1)(m+2)}{2m+3}, \end{aligned} \quad (\text{G3})$$

where we have used Legendre differential equations to substitute for the derivative of  $P'_{m+1}(\mu)$  in the third step and the orthogonality property of Legendre polynomials in the final step.

## H. BOUNDARY CONDITIONS FOR $F$ IN EQUATION (40)

We motivate the transformation of the variable from  $P$  to  $F$  by  $P = (1 - \mu^2)^{1/2} F$ . This enables us to write an ODE Equation (40) to solve directly for LL fields for all of the allowed cases of  $n$  that are numerically difficult to implement with the ODE for  $P$ , given by Equation (35). The angular part of the LL mode is given by Equation (35)

$$(1 - \mu^2)P'' + a^2 \frac{n+1}{n} P^{1+2/n} + n(n+1)P = 0. \quad (\text{H1})$$

We assume

$$P(\mu) = (1 - \mu^2)^\Gamma g(\mu), \quad (\text{H2})$$

as  $P(\mu = \pm 1) = 0$  for the highest possible  $\Gamma > 0$  such that  $g(\mu = \pm 1) \neq 0$ . Substituting for  $P$  in Equation (35) we obtain

$$\begin{aligned} (1 - \mu^2)^2 g'' + [-2\Gamma(1 - \mu^2) + 4\mu^2\Gamma(\Gamma - 1) + n(n+1)(1 - \mu^2)] g \\ - 4\mu\Gamma(1 - \mu^2)g' + a^2 \frac{(n+1)}{n} g^{\frac{n+2}{n}} (1 - \mu^2)^{\frac{2\Gamma}{n}+1} = 0. \end{aligned} \quad (\text{H3})$$

We now expand  $P$  using Equation (H2) in a power series of  $(1 - \mu^2)$  near  $\mu = \pm 1$ ,

$$P(\mu) = (1 - \mu^2)^\Gamma \sum_{\gamma=0}^{\infty} C_\gamma (1 - \mu^2)^\gamma, \quad (\text{H4})$$

where  $C_0$  is the leading term which is nonzero by definition. Comparing Equation (H2) and (H4), we can expand  $g(\mu)$  near  $\mu^2 = 1$  in a power series with coefficients  $C_\gamma$  as

$$\lim_{\mu^2 \rightarrow 1} g(\mu) = C_0 + C_1(1 - \mu^2) + C_2(1 - \mu^2)^2 + \dots \quad (\text{H5})$$

It is clear from above that in the limit  $\mu^2 \rightarrow 1$ ,  $g \rightarrow C_0$  which is a constant. Also we know that  $g'$  and  $g''$  are finite as  $\mu^2 \rightarrow 1$  because  $P(\mu)$  is finite in this limit. As a result, upon the substitution  $\mu^2 \rightarrow 1$ , Equation (H3) gives

$$4\mu^2\Gamma(\Gamma - 1)g = 0, \quad (\text{H6})$$

leading to  $\Gamma = 0, 1$ . The  $\Gamma = 0$  solution is not allowed whereas  $\Gamma = 1$  implies

$$P(\mu) = (1 - \mu^2)g = (1 - \mu^2)^{1/2} F. \quad (\text{H7})$$

Thus  $F$  satisfies the boundary conditions

$$F(\mu) = 0 \quad \text{at} \quad \mu = -1, 1. \quad (\text{H8})$$

## REFERENCES

- Amari, T., Aly, J. J., Luciani, J. F., Boulmezaoud, T. Z., & Mikic, Z. 1997, Sol. Phys., 174, 129
- Amari, T., Boulmezaoud, T. Z., & Aly, J. J. 2006, A&A, 446, 691
- Berger, M. A., & Field, G. B. 1984, Journal of Fluid Mechanics, 147, 133
- Berger, M. A. 1985, ApJS, 59, 433
- Chandrasekhar, S. 1956, Proceedings of the National Academy of Science, 42, 1
- Chandrasekhar, S., & Kendall, P. C. 1957, ApJ, 126, 457
- Chandrasekhar, S. 1961, International Series of Monographs on Physics, Oxford: Clarendon
- Finn, J. M., & Antonsen, T. M., Jr. 1983, Physics of Fluids, 26, 3540
- Comments Plasma Phys. Contr. Fusion, 9, 111
- Flyer, N., Fornberg, B., Thomas, S., & Low, B. C. 2004, ApJ, 606, 1210
- Grad, H. and Rubin, H. 1958, in Proc. 2nd Int. Conf. on Peaceful Uses of Atomic Energy, Vol. 31, Geneva: UN, 190
- Guo, Y., Ding, M. D., Wiegmann, T., & Li, H. 2008, ApJ, 679, 1629
- He, H., Wang, H., & Yan, Y. 2011, Journal of Geophysical Research (Space Physics), 116, 1101
- Ichimoto, K., Lites, B., et al. 2008, Sol. Phys., 249, 233
- Jing, J., Tan, C., Yuan, Y., et al. 2010, ApJ, 713, 440
- Leka, K. D., Barnes, G., & Crouch, A. 2009, The Second *Hinode* Science Meeting: Beyond Discovery-Toward Understanding, 415, 365
- Lites, B. W., & Skumanich, A. 1990, ApJ, 348, 747
- Lites, B. W., Elmore, D. F., Seagraves, P., & Skumanich, A. P. 1993, ApJ, 418, 928
- Low, B. C., & Lou, Y. Q. 1990, ApJ, 352, 343
- Low, B. C. 1996, Sol. Phys., 167, 217
- Low, B. C. 2006, ApJ, 646, 1288
- Mangalam, A., & Krishan, V. 2000, Journal of Astrophysics and Astronomy, 21, 299
- Marsh, G. E., 1996, Force Free Magnetic Fields: Solutions, Topology And Applications, World Scientific

- McClymont, A. N., & Mikic, Z. 1994, *ApJ*, 422, 899
- McClymont, A. N., Jiao, L., & Mikić. 1997, *Sol. Phys.*, 174, 191
- Metcalf, T. 1994, *Sol. Phys.*, 155, 235
- Metcalf, T. R., et al. 2006, *Sol. Phys.*, 237, 267
- Metcalf, T. R., et al. 2008, *Sol. Phys.*, 247, 269
- Park, S.-H., Chae, J., Jing, J., Tan, C., & Wang, H. 2010, *ApJ*, 720, 1102
- eds. Gopalswamy, N., Hasan, S. S., Rao, P. B., & Subramanian, P 2013, in *ASI Conf. Ser.* 10, 53
- Ravindra, B., & Howard, T. A. 2010, *Bulletin of the Astronomical Society of India*, 38, 147
- Ravindra, B., Yoshimura, K., & Dasso, S. 2011, *ApJ*, 743, 33
- Roumeliotis, G. 1996, *ApJ*, 473, 1095
- Schrijver, C. J., et al. 2006, *Sol. Phys.*, 235, 161
- Schrijver, C. J., De Rosa, M. L., Metcalf, T., et al. 2008, *ApJ*, 675, 1637
- Skumanich, A., & Lites, B. W. 1987, *ApJ*, 322, 473
- Taylor, J. B. 1974, *Physical Review Letters*, 33, 1139
- Venkatkrishnan, P., Hagyard, M. J., Hathway, D. H. 1988, *Sol. Phys.*, 115, 125
- Wheatland, M. S., Sturrock, P. A., & Roumeliotis, G. 2000, *ApJ*, 540, 1150
- Wheatland, M. S. 2007, *Sol. Phys.*, 245, 251
- Wheatland, M. S., & Régnier, S. 2009, *ApJ*, 700, L88
- Wheatland, M. S., & Leka, K. D., 2010, *ApJ*, 728, 112
- Wheatland, M. S., & Leka, K. D. 2011, *ApJ*, 728, 112
- Wiegelmann, T. 2004, *Sol. Phys.*, 219, 87
- Wiegelmann, T., Inhester, B., & Sakurai, T. 2006, *Sol. Phys.*, 233, 215
- Yang, W. H., Sturrock, P. A., & Antiochos, S. K. 1986, *ApJ*, 309, 383
- Yan, Y. and Sakurai, T.: 1997, *Sol. Phys.*, 174, 65.
- Yan, Y. and Sakurai, T.: 2000, *Sol. Phys.*, 195, 89.
- Yan, Y. 2005, *Space Sci. Rev.*, 121, 213



Yan, Y., & Li, Z. 2006, ApJ, 638, 1162

Zhang, M., Flyer, N., & Low, B. C. 2012, ApJ, 755, 78